Integration of submerged aquatic vegetation motion within hydrodynamic models

K Nakayama[1] T Shintani[2] K Komai[3] Y Nakagawa[4] JW Tsai[5] D Sasaki[1] K Tada[6] H Moki[7] T Kuwae[7] K Watanabe[7] MR Hipsey[8]

[1]*Graduate School of Engineering, Kobe University, 1-1 Rokkodai-cho Nada-ku, Kobe city, 658-8501, Japan*

[2]*Faculty of Urban Environmental Sciences, Tokuyo Metropolitan University, 1-1 Minami-Osawa Hachioji city, 192-0397, Japan*

[3]*Department of Civil and Environmental Engineering, Kitami Institute of Technology, 165 Koen-cho, Kitami 090-8501, Japan*

[4]*Graduate School of Engineering, Kyushu University, 744 Moto-oka Nishi-ku, Fukuoka 819-0395, Japan*

[5]*Department of Biological Science and Technology, China Medical University, No.91 Hsueh-Shih Road, Taichung, Taiwan*

[6]*Chuden Engineering Consultants, 2-3-30 Deshio, Minami-ku, Hiroshima 734-8510, Japan*

[7]*Coastal and Estuarine Environment Research Group, Port and Airport Research Institute, 3-1-1, Nagase, Yokosuka 239-0826, Japan*

[8]*Aquatic Ecodynamics, UWA School of Agriculture and Environment, The University of Western Australia, Australia*

Corresponding author: Keisuke Nakayama (nakayama@phoenix.kobe-u.ac.jp)

Key Points:

- A model is presented to capture the changing position of Submerged Aquatic Vegetation blades in response to flow, and validated using laboratory experiments.
- Forcing terms that control seagrass movement within a meadow are evaluated.
- Estimates of deflected vegetation height and bulk meadow friction coefficients demonstrate the importance of simulating SAV motion in lakes and coastal areas.

Abstract

Aquatic models used for both freshwater and marine systems frequently need to account for submerged aquatic vegetation (SAV) due to its influence on flow and water quality. Despite its importance, simplified parameterizations are generally adopted that simplify feedbacks between flow, canopy properties (e.g., considering the deflected vegetation height) and the bulk friction coefficient. This study reports the development of a fine-scale non-hydrostatic model that demonstrates the two-way effects of SAV motion interaction with the flow. An object-oriented approach is used to capture the multiphase phenomena, whereby a leaf-scale SAV model based on a discrete element method is combined with a flow-dynamics model able to resolve stresses from currents and waves. The model is verified through application to a laboratory-scale seagrass bed. A force balance analysis revealed that leaf elasticity and buoyancy are the most significant components influencing the horizontal and vertical momentum equations, respectively. The sensitivity of canopy-scale bulk friction coefficients to water depth, current speeds and vegetation density of seagrass was explored. Deeper water was also shown to lead to larger deflection of vegetation height. The model approach can contribute to improved assessment of processes influencing, water quality, sediment stabilization, carbon sequestration, and SAV restoration, thereby supporting understanding of how waterways and coasts will respond to changes brought about by development and a changing climate.

1 Introduction

Climate change mitigation and adaptation strategies are urgently needed (IPCC, 2014) to reduce the negative impacts associated with natural disasters, such as flood inundation and landslides (Hirabayashi et al. 2013; Tezuka et al. 2013), biodiversity loss (Thuiller, 2007, Dutta

et al. 2013), and land and water degradation (Nakayama et al., 2010; Fragoso et al., 2011; Sachse et al., 2014; Me et al., 2018; Song et al. 2018). Restoration of submerged aquatic vegetation (SAV) in aquatic ecosystems has been suggested as a potential mitigation strategy (Nellmann et al., 2009). For example, whilst shallow coastal areas have often been assumed to release carbon dioxide to the atmosphere due to inputs of organic matter from rivers (Cai, 2011; Adiyanti et al., 2016), well-vegetated aquatic environments have recently been shown to absorb and capture carbon dioxide - a potential sink of anthropogenic carbon as sedimentary organic carbon, termed "blue carbon" (Duarte et al., 2013). Nellemann et al. (2009) reports that coastal blue carbon ecosystems accumulate approximately 55 % of the total carbon dioxide captured from the Earth's atmosphere due to photosynthesis. Whilst there is empirical evidence for blue carbon capture in seagrass systems, sequestration rates are highly variable (Lavery et al., 2013), and the conditions that can enhance or disrupt carbon capture and storage remains of topical interest. Similarly in inland waters, SAV has also been revealed to stabilize water quality in rivers (Weitzman et al., 2013), shallow lakes (Hilt et al., 2018), and potentially also within deep lakes (Sachse et al. 2014). A more accurate understanding of the hydrodynamic environment associated with SAV and the various water-vegetation-sediment feedbacks could improve our estimation of carbon storage potential, and allow us to devise optimal restoration approaches of SAV in degraded waterbodies (e.g., Adams et al., 2018; Prentice et al., 2019).

Given the wide diversity of vegetation forms and hydrologic contexts, numerical models serve an important role to resolve the interaction of SAV with hydrodynamic flows and biogeochemical cycles and to support the management and restoration of SAV communities (Macreadie et al., 2014). To date, the inclusion of SAV within Aquatic Ecosystem Models (AEMs) has focused on either a) the effect of vegetation on flow hydrodynamics, since the

vegetation canopy induces drag to the passing flow and affects the water circulation (Weitzman et al., 2015; Zeller et al., 2014), and/or b) the role of vegetation in aquatic biogeochemical cycling in the water and sediment (Trolle et al., 2014; Baird et al., 2016). In both cases the more complex feedbacks between vegetation movement and aquatic system response has yet to be fully accounted for, at least in hydrodynamic-biogeochemical models applied at scales relevant for integrated assessment (Adams et al., 2016; Abdolahpour et al., 2018).

As the vegetation itself can modify the hydrodynamic conditions within a water body (Lacy and Wylie-Echeverria, 2011), depending on plant morphological form and organization of the canopy (e.g., Boothroyd et al., 2016), it must also be acknowledged that individual plants within a meadow may not all behave identically. A number of laboratory studies where the behaviour of each shoot and leaf blade has been considered have demonstrated the importance of plant flexibility (Abdolahpour et al. 2018), and, in general, it has been shown that stiff leaves exhibit a higher drag force than more than flexible leaves (Bouma et al., 2005). Mass transport in more flexible canopies has been shown to increase downstream due to enlargement of the exchange zone (Murphy et al., 2007; Ghisalberti and Nepf, 2009). Furthermore, residual currents in the opposite direction to the progressive direction of waves adjacent to the water surface have been found to occur because of wave set up at the upstream edge of the canopy (Luhar et al., 2010). Interactions between SAV canopy dynamics and flow have historically been evaluated based on the extent of the flow-induced reconfiguration of aquatic vegetation using the Cauchy number (Ca) and the Buoyancy parameter (B) (Luhar and Nepf, 2011; Nepf, 2012; Whittaker et al., 2015; Luhar and Nepf, 2016). Ca indicates the relative magnitude of the drag force and elasticity, computed as $\mathrm{Ca} = \rho C_D b U^2 l^3/(2EI)$, where ρ is the density of water, C_D is the drag coefficient, b is the width of blade leaf, U is the horizontal velocity, l is the blade leaf length, E

is the elastic modulus, and I is the second moment of inertia. B indicates the relative magnitude of the buoyancy and elasticity, computed as $B = \Delta\rho g\ b\ t_h\ l^3/(EI)$, where $\Delta\rho$ is the density difference between the water and the blade leaf, and t_h is the thickness of blade leaf. These dimensionless parameters have been successfully applied to describe results from field scale case studies (e.g., Luhar and Nepf, 2013).

In parallel, there have been various numerical approaches developed to account for the effect of SAV within hydrodynamic models. The most common has been to apply traditional flow resistance formulae in a hydrodynamic model, such as use of a bulk friction coefficient (e.g. Manning's roughness), and another has been to develop a coupled hydrodynamic-SAV model under the condition that there is a vegetation "element" per computational horizontal-cell (Wilson et al., 2006; Wilson et al., 2007). In general, the first approach adopts a hydrostatic approximation and is suited to field scale analyses since the horizontal mesh size is coarse and much larger than a vegetation element. For example, Vilas et al. (2017) demonstrated that spatial and temporal patterns of dissolved oxygen concentrations and associated effects on nutrient cycling were able to be adequately captured by including the bulk effect of macrophytes in a three-dimensional shallow lake model. The latter approach provides more detail of the flow-vegetation interaction (Suzuki et al., 2011; Infantes et al., 2012; Boothroyd et al., 2016), however, demands finer grid resolution which can considerably increase computational cost when applying it to environmental systems at larger scales.

To evaluate spatio-temporal variability in vegetation deflection and changes in the canopy bulk friction coefficients under varied hydraulic conditions, a dynamic SAV model can account for the feedbacks between vegetation movement and environmental conditions (Stoesser et al., 2003; Anderson et al., 2006; Noarayanan et al., 2012; Li et al., 2014; Busari and Li, 2015).

This necessitates developing methods for integrating individual SAV behavior within hydrodynamic models, to support improved environmental modelling at realistic field scales required for carbon and nutrient budgeting and restoration decision–making (Guan and Liang, 2017). At the individual plant scale, there have been several key studies where the movement and position of each leaf blade are modelled by considering the interaction with the current and wave field (Kutija and Hong, 1996; Verduin and Backhaus, 2000; Abdelrhman, 2007; Dijkstra and Uittenbogaard, 2010; Marjoribannks et al., 2014; Gac, 2014). In Abdelrhman's 2007 eelgrass model, individual blades were divided into separate segments, each subject to drag force, lift force, friction force and buoyancy. This approach was found to agree well with laboratory experiments, and the authors successfully reproduced the shelter effect originally noted in Seginer et al. (1976), though it did not include elastic forces, which Nepf (2012) experimentally demonstrated as one of the most important factors shaping the profile of seagrass. Dijkstra and Uittenbogaard (2010) applied a similar method as Abdelrhman (2007) by including the modulus of elasticity with good agreement to laboratory experiments, and Marjoribanks et al. (2014) demonstrated an accurate high-resolution hydrodynamic model able to include interactions between flow and river vegetation by accounting for plant rigidity and employing Large Eddy Simulation (LES) to examine turbulence properties in detail. Open questions remain, however, related to simulation of flexible vegetation, both related to theoretical questions, such as the effect of vegetation density, form and meadow characteristics on vegetation and the flow, and also methodological questions related to model validation, and numerical approaches for addressing scaling and stability issues.

Object-oriented programming (OOP) methods can enable the easy combination of multiphase phenomena and the development of integrated environmental modelling (Laniak et

al., 2013; Turuncoglu et al. 2013), thereby providing an opportunity to better resolve SAV within AEMs across diverse contexts. As an initial step towards this goal, the aim of this study was to develop a fully-coupled hydrodynamic-SAV model, using an OOP approach, verified with laboratory experiment data. Firstly, a new individual blade-based SAV model is proposed for seagrass, based on the Discrete Element Method (DEM), considering drag, lift, friction and elastic forces, and buoyancy. A new computational approach for linking the Lagrangian seagrass blade dynamics with the flow fields predicted by a three-dimensional environmental fluid dynamics model (Fantom), is introduced. The coupled Fantom-SAV model is validated by comparing with experimental data on vegetation form during uniform channel flow, and the contribution of each force to vegetation dynamics is investigated under different conditions. Finally, for analyzing field scale phenomenon, velocity, deflected vegetation height and bulk friction coefficients of seagrass meadows were explored. The approach presented is a necessary step to facilitate simulation of improved flow-vegetation-sediment feedbacks in AEMs, and can be used to support scenario modelling of SAV dynamics in aquatic systems.

2 Materials

2.1 SAV model

Using the DEM approach, each leaf can be divided into connected separate segments, which together are used to compute the Lagrangian blade dynamics. This approach is different from Abdelrhman (2007) and the other model studies reported above who adopt a continuous representation, making it more convenient for combining with a non-hydrostatic hydrodynamic model (Figure 1). The acceleration of the elements is resolved based on the individual force components, including the drag, lift and friction forces from the flow, the buoyancy of seagrass,

and the elastic force associated with leaf stretching. All forces associated with the interaction with the flow are assumed to apply at the node that connects each segment, in order to obtain node velocities, and we apply a limiting condition of a constant length of the segment. Since the node velocities of the separate leaf blade segments are solved for using the DEM approach, the SAV model must be combined with a three-dimensional hydrodynamic model via an interface that maps the flow velocity from the hydrodynamic model mesh at the appropriate location, and returning the friction and drag terms to the Navier-Stokes equations accordingly.

In total, the SAV model equation for horizontal motion of each node is:

$$\rho_S V_S \frac{du_S}{dt} = \underbrace{\rho_w \frac{|\mathbf{u}-\mathbf{u_s}|(u-u_S)}{2} C_D A_z}_{\text{drag force}} + \underbrace{\rho_w \frac{|\mathbf{u}-\mathbf{u_s}|(u-u_S)}{2} f_C A_x}_{\text{friction force}} \underbrace{-EIL_S \frac{\partial^4 \zeta_S}{\partial z^4}}_{\text{elastic force}} \quad (1)$$

and for vertical motion:

$$\rho_S V_S \frac{dw_S}{dt} = \underbrace{\rho_w \frac{|\mathbf{u}-\mathbf{u_s}|(w-w_S)}{2} C_D A_x}_{\text{drag force}} + \underbrace{\rho_w \frac{|\mathbf{u}-\mathbf{u_s}|(w-w_S)}{2} f_C A_z}_{\text{friction force}} + \underbrace{\rho_w \frac{C_L}{2} |\mathbf{u}-\mathbf{u_s}|^2 A_z}_{\text{lift force}} + \underbrace{(\rho_w - \rho_S) g V_B}_{\text{buoyancy}} \quad (2)$$

where t is the time (s), V_S is the volume of a segment (m^3), L_S is the length of a segment (m^3), ρ_S is the density of seagrass (kg m^{-3}), ρ_w is the density of water (kg m^{-3}), $\mathbf{u}$ is the vector of current (m s^{-1}), $\mathbf{u_S}$ is the vector of a node (m s^{-1}), u is the horizontal velocity of the current (m s^{-1}), u_S is the horizontal velocity of a seagrass node (m s^{-1}), C_D is the drag coefficient, A_z is the vertically projected area (m^2), f_C is a friction coefficient, A_x is the horizontally projected area (m^2), E is the elastic modulus (Pa), I is the second moment of inertia (m^4) , ζ_S is the displacement of a node (m), w_S is the vertical velocity of a node (m s^{-1}), w is the vertical velocity of the current (m s^{-1}),

C_L is the lift force coefficient, g is the acceleration due to gravity (m s^{-2}), and V_B is the buoyancy volume (m^3).

2.2 Integration of SAV model into the flow dynamics model

The interaction between seagrass and flow is analyzed and evaluated by coupling the SAV model (equations (1) and (2)) with the hydrodynamic model Fantom (Nakayama et al., 2014; Nakayama et al., 2016; Nakayama et al., 2019). The Fantom code applies the predictor-corrector method to compute the non-hydrostatic effects on flow (Nakayama, 2006; Nakayama and Imberger, 2010; Nakayama et al., 2012), and a generic *k*-ε length-scale turbulent closure model (Umlauf and Burchard, 2003), which is used with a CA filter (Warner et al., 2005). Drag and friction forces brought about by the leaf blade interaction with the flow field are included in Fantom to take into account the reaction from the leaf to the horizontal and vertical velocity components:

$$M_x = -\rho_w \frac{|\mathbf{u} - \mathbf{u_s}|(u - u_S)}{2}(C_D A_z + f_C A_x) \tag{3}$$

$$M_z = -\rho_w \frac{|\mathbf{u} - \mathbf{u_s}|(w - w_S)}{2}(C_D A_x + f_C A_z) \tag{4}$$

where M_x is the additional horizontal momentum from the leaf blade (kg m s^{-2}), and M_z is the additional vertical momentum from seagrass (kg m s^{-2}).

Fantom has been developed based on OOP, and the initial and boundary conditions are all controlled using the *lua* language. Parallel computing is available as a byproduct of the OOP design (Figure 2). In the numerical procedure, the first prediction step is the flow component calculation. In the second step, the predicted flow velocities are used to calculate the moving speed of the leaf nodes based on the DEM. Finally, in the corrector step, the Poisson equation is

205 solved to obtain flow velocities which satisfy the continuity equation, and all values are used in
206 the next step, with a time step of Δt.

207 In the second step of the SAV model, seagrass leaf objects find the respective mesh cells
208 that correspond to each node of the leaf adjacent to the bottom, and retrieves the flow velocities
209 for the x and z coordinate, u and w. By using equations (1) and (2), u_S and w_S of the node at the
210 next time step are computed, respectively, and, the node locations of the x and z coordinate are
211 updated by using the velocity of the node. At this stage, we apply a limiting condition of a length
212 of the segment, and then computation of the position of the remaining nodes is done from the
213 second node from the bottom to the tip of the seagrass leaf, for all seagrass blades. After
214 finishing the seagrass leaf motion computation, the mesh cell indices that correspond to all nodes
215 of the leaf objects are identified. Lastly, the flow velocities within the mesh, u and w, are updated
216 accounting for the momentum sink computed using equations (3) and (4).

217 *2.3 Laboratory experiment description*

218 To assess the model, flow in an open channel tank planted with seagrass that was
219 sampled from the Akkeshi-ko estuary in north-eastern Hokkaido, Japan, was used. The seagrass
220 was eelgrass, *Zostera marina*, which was kept refrigerated during transportation to ensure there
221 was little change in the properties of the seagrass prior to the laboratory experiments. Four
222 experiments were conducted soon after receiving the eelgrass samples. The tank had a water
223 depth of 0.7 m, width of 0.7 m, and length of 5.0 m, and unidirectional flow was induced using a
224 pump (Figure 3). The seagrass was deployed over an area within the tank with a length of 1.5 m,
225 as shown in Figure 3. The vegetation density of seagrass was 1/0.01 shoot m^{-2}, and each shoot
226 had 4 leaves with a blade length of 1.0 m for cases 1 and 2, and with a blade length of 0.35 m for
227 cases 3 and 4, respectively (Table I). The average width of a seagrass leaf was 0.010 m, such that

the leaf area of one-side was 0.01 m^2 in cases 1 and 2, for each blade, and 0.0035 m^2 in cases 3 and 4. The thickness of a seagrass leaf was estimated as 0.001 m, and the areal leaf biomass was set based on sampling *Z. marina* from a vegetated brackish lake, (Lake Komuke located in north-eastern Hokkaido near to Akkeshi-ko estuary), which was estimated to be approximately 200 g DW m^{-2} by using the leaf area of both sides of the leaf (m^2). A video measurement system was applied to monitor the profile of seagrass, and an Acoustic Doppler Velocimeter (ADV) was used to measure velocity at a height of 0.3 m in front of the seagrass (no.1 in Figure 3), and behind the seagrass (no.2 in Figure 3). Two different mean flows of 0.08 m s^{-1} and 0.04 m s^{-1} were induced in cases 1 and 3, and cases 2 and 4, respectively, in order to investigate the sensitivity to the unidirectional flow velocity.

2.4 Calibration and verification of the SAV model

Several model simulations were configured to reproduce the experimental results. Since unidirectional currents were forced from the left side of the laboratory setup (see Figure 3), similar currents were applied as a boundary condition at the left side of the computational domain in the numerical model. To give the same conditions, in which there is no wave reflection from the right-side boundary, the length of the computational domain was set to 250 m. Seagrass was located between 32 m and 33.5 m from the left-side boundary in order to give stable unidirectional currents. If we assume that the energy transfers by following the maximum wave speed, it is expected to take about $466.5/(9.8\times0.7)^{-0.5}$ = 178 s for energy to propagate from the left to right-side boundary, and reflect from the right side boundary to the seagrass. Since the seagrass reached a steady state 40 s, based on the video images after the initial currents commenced, 178 s is considered sufficient to analyze appropriate seagrass motions without the influence of reflection from the right-side boundary. It was confirmed that there was no

significant difference in flow fields and seagrass motion across the channel width. Therefore, the vertically-resolved two-dimensional computation was applied by giving a width of 0.1 m for the 1/0.01 shoot m^{-2} case, with a slip condition on the lateral walls. The width of the computational domain was altered depending on the vegetation density of seagrass. The number of leaves in each shoot was given as 4 and the length as 1.0 m and 0.35 m for cases 1 to 2 and cases 3 to 4 (Table I). Because the computational domain length was 250 m to remove the effect of reflection from the right-side boundary, the horizontal size of the mesh was changed. The minimum horizontal mesh size was 0.05 m around the seagrass which changed from 0.10 m, 0.20 m 0.25 m, 0.50 m and 1.00 m towards the right-side boundary. The vertical mesh size was 0.02 m from the bottom to a height of 0.10 m and 0.05 m elsewhere. The timestep was 0.0025 s.

We tested several parameter combinations with the SAV model to calibrate the drag coefficient, friction coefficient, lift force coefficient, and elastic modulus. The drag, lift force and friction coefficients were set as shown in case Lab1 of Table II (case 1 in Table I) by following Abdelrhman (2007). The elastic modulus and buoyancy were determined by trial and error, with case Lab1 giving the best fit to the laboratory results. Luhar et al. (2011) showed the range of elastic modulus of *Zostera marina* to be between 0.4 and 2.4 GPa, which is smaller than this study. This may be because their eelgrass length is from 0.3 m to 0.5 m and is younger than the eelgrass used in our trials. To verify the validity of the coefficients, the profile of seagrass and the velocity in front and behind the seagrass meadows was compared between laboratory experiments and numerical computations for cases 2 to 4 in Table I.

2.5 Sensitivity analysis of SAV model

To elucidate the contribution of elastic modulus, drag, friction and lift force coefficients to the seagrass motion and flow behavior, the profile of seagrass leaves and the velocity on either side of the seagrass meadows was compared for cases Lab1 to Cl_L as in Table II. To test the sensitivity of elastic forces, 75 % and 125 % of the elastic modulus values were compared to case Lab1 in cases E_S and E_L, respectively. Similarly, for investigating the contribution of drag, friction and lift force coefficients, 50 % and 150 % coefficients were compared to case Lab1 in cases Cd_S to Cl_L. It should be noted that different percentages were given in cases E_S and E_L compared to cases Cd_S to Cl_L because the contribution of the elastic modulus was larger relative to the other coefficients, as shown in sections 3.1 and 3.2. Furthermore, the detailed contribution of elastic, drag, friction and lift forces was quantified for the Lab1 case.

2.6 Field scale assessment

To analyze dynamics within a field scale setting, we carried out a simulation setup with a larger seagrass meadow. Seagrass was set up in a region with a length of 15 m, which was chosen by using the length scale for transition when boundary-layer flow changes to mixing-layer-type flow (Ghisalberti and Nepf, 2009). The total length of the computational domain was 250 m, and the horizontal mesh size changed following the same pattern as the laboratory experiment computation cases, from 0.05 m, 0.10 m, 0.20 m, 0.25 m, 0.50 m and 1.00 m. The vertical mesh size was 0.02 m from the bottom to a height of 0.10 m and 0.05 m elsewhere. Seagrass was set up from 32 m to 47 m from the left-side boundary. The length of the seagrass leaves was set to 1.0 m, with the other conditions the same as the laboratory experiment simulation cases (case Lab1 of Table II).

294 In general, the water depth, unidirectional flow speed and vegetation density of seagrass
295 shoots can vary considerably in a field situation. Therefore, we explored a total of 12 cases,
296 covering three different water depths, 0.50 m, 1.0 m and 1.5 m, two different unidirectional
297 velocities, 0.05 m s^{-1} and 0.10 m s^{-1}, and two different densities of seagrass shoot, 1/0.0225 shoot
298 m^{-2} and 1/0.01 shoot m^{-2}, respectively (Table III). In the analysis, we calculated the deflected
299 vegetation height as outlined in Luhar and Nepf (2011), and flow velocities inside and above the
300 meadow were summarized and the bulk friction coefficient over the seagrass meadow was
301 estimated.

302

303 **3 Results**

304 *3.1 Model assessment and sensitivity*

305 To validate the SAV model performance, the profile of seagrass was calculated in front
306 and behind the seagrass meadows for the cases 1 to 4 for unidirectional currents. All coefficients,
307 drag coefficient, friction coefficient, lift force coefficient, and elastic modulus, were determined
308 by applying the SAV model into case 1 (case Lab1), and the other cases, cases 2 to 4, were
309 applied to verify the SAV model by using the same coefficients. The profiles showed very good
310 agreement with the all laboratory experiments (Figure 4). The positions for horizontal and
311 vertical coordinates were chosen every 0.2 m from the bottom to the top of seagrass, and R^2 =
312 0.99 for Xb and R^2 = 0.97 for Zb, respectively. Also, the horizontal velocities agreed well with
313 the laboratory experiments although the horizontal velocity behind the seagrass meadow was
314 overestimated slightly (Figure 5).

315 The influence of the elastic modulus, drag coefficient and friction coefficient on
316 horizontal velocity was investigated (Figure 6). When the elastic modulus decreased in case E_S

compared to case E_L, the leaves were more bent and a larger volume of free flow conditions was possible above the meadow, resulting in a smaller velocity above the canopy (Figures 6(b) and 6(c)). On the other hand, when the drag coefficient increased in case Cd_L, compared to case Cd_S, the seagrass blades bent more and smaller horizontal velocities occur inside the meadow (Figures 6(d) and 6(e)). Although the same tendency was found when changes to the friction coefficient are made, the sensitivity of the friction coefficient was smaller than the drag coefficient (Figures 6(f) and 6(g)).

3.2 Controls on variability of seagrass forces

To quantitatively evaluate the contribution of all forces on seagrass blades, all terms of the SAV model equations were calculated in front, inside and behind the seagrass meadows for 75 s from the initial conditions (Figure 7). For the horizontal momentum, drag, friction and elastic forces were considered as follows:

$$M^*\text{cd\_h} = \frac{\rho_w}{\rho_S V_S}\frac{|\mathbf{u}-\mathbf{u_s}|(u-u_S)}{2}C_D A_z \tag{5}$$

$$M^*\text{fc\_h} = \frac{\rho_w}{\rho_S V_S}\frac{|\mathbf{u}-\mathbf{u_s}|(u-u_S)}{2}f_C A_x \tag{6}$$

$$M^*\text{ei\_h} = -\frac{EI}{\rho_S V_S}\frac{\partial^3 w_S}{\partial z^3} \tag{7}$$

Similarly, for the vertical momentum, drag, friction, lift forces and buoyancy were computed according to:

$$M^*\text{cd\_v} = \frac{\rho_w}{\rho_S V_S}\frac{|\mathbf{u}-\mathbf{u_s}|(w-w_S)}{2}C_D A_x \tag{8}$$

$$M^{*}\text{fc\_v} = \frac{\rho_w}{\rho_S V_S}\frac{|\mathbf{u}-\mathbf{u_s}|(w-w_S)}{2} f_C A_z \tag{9}$$

$$M^{*}\text{ei\_v} = \frac{\rho_w}{\rho_S V_S}\frac{C_L}{2}|\mathbf{u}-\mathbf{u_s}|^2 A_x \tag{10}$$

$$M^{*}\text{bu\_v} = \frac{\rho_w-\rho_s}{\rho_S V_S} g V_B \tag{11}$$

The maximum drag, friction and elastic forces were found to appear at the front of the seagrass meadows for horizontal momentum (Figures 7(a) to 7(c)). The contribution of the friction force was minimal compared to the drag and elastic forces. Since the largest contribution to seagrass profile is the elastic force, the elastic modulus was found to be one of the most significant coefficients controlling the horizontal momentum.

For vertical momentum, the largest contribution to the seagrass leaf profile was buoyancy, followed by lift forces. The contribution of lift forces to seagrass was almost the same in front, inside and behind the meadow. The drag force inside the meadow was close to zero, although drag forces in front and behind the meadow had larger values. Friction forces were negligible in the vertical momentum balance.

3.3 Deflected vegetation height prediction at the field scale

To investigate the interaction between seagrass meadows and flow at field scales, 15 m meadow of seagrass was set up in a SAV model simulation, with water depth, unidirectional currents and vegetation density configured as shown in Table III. Figure 8 is an example of computational results of case w15v05d_L. Deflected vegetation height was constant in cases w05v05d_L and w05v05d_S because the leaves reached the water surface (Figure 9). When we pay attention to the same unidirectional current cases, for example case w05v10d_L, case w10v10d_L

348 and case w15v10d_L, the deflected vegetation height was found to increase with an increase in the
349 total water depth because there is more room above the seagrass canopy in a larger total water
350 depth. Furthermore, for lower vegetation densities, there was a proportionally smaller deflection
351 in the vegetation height. Also, the deflected vegetation height was confirmed to become constant
352 at a distance of 1 to 2 m from the front of the seagrass meadows.

353 *3.4 Velocity field*

354 Horizontal velocity was investigated inside and above the seagrass meadows (Figure 10).
355 In the shallowest cases, a water depth of 0.5 m, horizontal velocity inside and above the seagrass
356 was found to be constant at a distance of 3 m from the front of the meadow. Under the medium
357 water depth case, a water depth of 1.0 m, when the unidirectional current speed was 0.05 m s^{-1},
358 horizontal velocity inside and above the seagrass was constant at a distance of 10 m from the
359 front of the meadow. In the deepest case, a water depth of 1.5 m, horizontal velocity inside and
360 above the seagrass did not reach a constant value. Therefore, a constant horizontal velocity inside
361 and above the meadows may occur more quickly when the unidirectional current speed is smaller
362 and water depths are shallower. Furthermore, even though the currents were the same, deeper
363 water led to smaller horizontal velocities inside the meadow itself.

364 *3.5 Friction coefficient within a uniform current*

365 It is useful to evaluate bulk friction coefficients for a lakes or coastal systems, where the
366 effects of vegetation need to be parameterized in large-scale models. Therefore, we made an
367 attempt to estimate the bulk friction coefficients above seagrass meadows using the eddy
368 viscosity and vertical profile of horizontal velocity. For example, the vertical profile of
369 horizontal velocity obtained in cases w15v05d_L to w15v10d_S is shown in Figures 11(d) and
370 11(e). The shear stress at the top of seagrass, τ_S (kg m^{-1} s^{-2}), was obtained using:

$$\tau_S = \rho_w K_M \frac{\partial u}{\partial z} \tag{12}$$

where K_M is the eddy viscosity obtained from k-ε model ($m^2\ s^{-1}$). The shear stress can be modelled by introducing friction coefficients above the seagrass meadow, which may yield the bulk friction coefficient as:

$$\frac{\tau_S}{\rho_w} = f_S |\boldsymbol{u_w}| u_w \tag{13}$$

$$f_S = \frac{K_M}{|\boldsymbol{u_w}| u_w} \frac{\partial u}{\partial z} \tag{14}$$

where f_S is the bulk friction coefficient and u_w is the depth averaged horizontal velocity above seagrass ($m\ s^{-1}$).

Bulk friction coefficients for a water depth of 0.5 m were obtained around 0.02 at the end of the seagrass meadows for both densities of seagrass, 1/0.01 shoot m^{-2} and 1/0.0225 shoot m^{-2} (Figure 11). For a water depth of 1.0 m, bulk friction coefficients reached a constant value when unidirectional current speeds were 0.1 m s^{-1} though the bulk friction coefficient increased at the end of the seagrass meadows for a unidirectional current speed of 0.05 m s^{-1}. For a water depth of 1.5 m, the bulk friction coefficient reached a constant value when unidirectional current speeds were 0.05 m s^{-1}. For all cases, the bulk friction coefficient increased with decreasing unidirectional current speeds, increasing vegetation density of seagrass, and increasing water depth. In particular, bulk friction coefficients were confirmed to reach 0.049 for case $w15v05d_L$ with a unidirectional current speed of 0.05m s^{-1}, vegetation density of 1/0.01 shoot m^{-2} and a water depth of 1.5 m. A bulk friction coefficient of 0.049 is 20 times that of the smooth bottom friction value of 0.0026.

4 Discussion

We have demonstrated that an OOP based model framework can be used to successfully couple a Lagrangian SAV model with a hydrodynamic model to characterize the flexible nature of individual leaves within a meadow, in response to the biophysical environment. The performance of our SAV model was confirmed through comparison of laboratory experiments with unidirectional currents, with good agreement in the profiles of leaf blade position and flow velocity. This model results reveal the quantitative influence of elastic modulus, drag, friction, and lift forces, and buoyancy on flow fields around meadows of submerged vegetation. The elastic force was found to be the most influential component in the interaction between horizontal currents and seagrass, whereas buoyancy was revealed to be the most significant term in the vertical momentum balance. The simulation approach adopted here for elasticity is different from the earlier approaches, whereby rigidity is computed as the second derivative of curvature, tempered by a damping factor to manage instability (Marjoribanks et al., 2014). Here elasticity was captured by approximating the local curvature using backward difference. The speed of SAV nodes is the variable in the basic equations of our model based on DEM although the variable in DEM is the location of an element. Since the fluid is solved by using the fluid velocities, this technique gives computational stability.

The development of a boundary layer around the top of the seagrass meadow was characterized and confirmed using field scale simulations; the lateral variation in the boundary layer would not be accurately captured in models assuming static and rigid seagrass presence. Simulations showed that larger water depths were found to lead to larger deflection of vegetation height. In previous studies, Ca and B have been applied to estimate deflected vegetation height

411 and so we made comparisons with the theoretical solutions (Luhar and Nepf, 2011). The leaf
412 blade parameters were set as $l = 1.0$ m, $b = 0.01$ m, $t = 0.001$ m, $\Delta\rho = 0.005$, $C_D = 1.0$, and
413 $EI = 2.79 \times 10^{-4}$ N m^2, and, in the numerical computations, one blade leaf was given with
414 $f_c = 0.30$ and $C_L = 0.10$. For a horizontal velocity of 0.10 m s^{-1}, the theoretical deflected
415 vegetation height is 0.37 m. Since it was shown in this study that water depth influences the
416 deflected vegetation height, three alternate water depths were compared: 0.5 m, 1.0 m and 1.5 m;
417 these result in the deflected vegetation heights of 0.28 m, 0.31 m and 0.33 m, respectively. As
418 shown in Figure 9, the larger water depth case tends to be similar to the theoretical solution,
419 which provides a reasonable estimate of the deflected vegetation height.

420 The adoption of a turbulent closure model also allowed estimation of bulk friction
421 coefficients over seagrass using the vertical profile of horizontal velocity. This showed that bulk
422 friction coefficients increase with increasing water depth, decreasing current speeds, and
423 increasing leaf blade density. The maximum bulk friction coefficient obtained from the dynamic
424 model in this study was 0.049, comparable to Ghisalberti and Nepf (2006) and Luhar et al.
425 (2013) who suggested that 0.05 (=2f_S) should be applied in three-dimensional simulations. By
426 looking closer at case w15v05d$_L$, a typical boundary layer is notable along the top of the
427 seagrass meadow (Figure 8). The integral length-scale obtained from the generic length-scale
428 turbulent closure model, l_T, was found to increase from the front of the meadow up to 0.27 m,
429 after which it remains constant until the end, similar to the boundary layer demonstrated in
430 Ghisalberti and Nepf (2009). Whilst LES is increasingly popular in laboratory scale applications
431 to more accurately compute the interaction between turbulent eddies and vegetation at high
432 resolution (e.g., Marjoribanks et al., 2014), it can be computationally expensive to resolve eddies
433 up to the inertial sub-range of the turbulence for field scale problems. Our results give

confidence that the use of more simple closure models remains accurate, whilst also being practical across a wider range of scales. Ultimately, having flexibility to be able to apply different closure options and model resolutions can support model applicability across a wider range of phenomena from lab to field scales, and the OOP approach used in the Fantom-SAV model development is useful in that it can support testing of different computational approaches, closure options and mesh resolutions whilst maintaining a standard coupling interface to the Lagrangian SAV model.

Whilst the focus here has been on the physical interaction of the benthic vegetation with the flow field, the model approach has significant potential for extension to applications associated with the analysis of carbon capture and burial, and for improved prediction of nutrient and contaminant fluxes that may impact upon water quality. For example, when elastic forces are smaller, greater bend in leaf blades causes larger decreases in velocity inside of seagrass meadows, which results in the enhancement of accumulation of particulate organic carbon and nutrients (Duarte et al., 2013). Therefore, if there is no bend in the leaf blades, the rate of carbon and nutrient accumulation rate may decrease. As an example, we compared the case $w15v05d_L$ condition with a hypothetical no-seagrass-motion equivalent simulation. With no bend in the leaf blades, the friction coefficient 6 m from the meadow front increases from 0.032 to 0.039, about 20% increase (Figure 12). Additionally, flow velocity adjacent to the bottom, which controls resuspension of the bottom sediments, is smaller with seagrass motion than without seagrass motion (Figures 12(b)). For example, the horizontal velocity at the height of 0.15 m is 0.045 (m s^{-1}) with seagrass motion and increases to 0.057 (m s^{-1}) without seagrass motion, a 27% difference. There are also notable differences in horizontal velocity around the top of the seagrass meadow (Figure 12(b)). Therefore, if seagrass motion is not included in numerical

model simulations, the bulk friction coefficient is underestimated and resuspension from the bottom, will be overestimated. In real seagrass meadows, the area of meadow downstream of the edge is notably larger than the edge areas, and therefore it is expected to dominate the amount of vertical flux, friction and resuspension (Marjoribannks et al., 2014; Boothroyd et al., 2016). Overall, accounting for the bend in the leaf blades is likely to be important for evaluating friction, vertical fluxes and resuspension around complex meadow geometries in the environment and further applications of the model could be to explore the feedbacks between water flow regimes, vegetation properties and sediment dynamics (Adams et al., 2018).

As with earlier approaches, scaling up the model approach to large-scale environmental systems remains challenging, though applications where the model is applied to evaluate detailed flow fields around SAVs, provide opportunities to parameterize reduced models of deflected vegetation height and bulk friction coefficients under various hydraulic conditions. Such approaches can be adopted into large-scale three-dimensional environmental models that adopt a relatively coarse mesh resolution compared to the size of the vegetation elements to allow the essential feedbacks to be captured whilst maintaining tractability.

Although this study has focused on investigating the effect of simple linear seagrass blade morphometries on flow fields, the DEM method developed in this study has been developed as a first step towards simulations of SAV communities made up of more morphometrically complex and diverse vegetation elements. Boothroyd et al. (2016), recently highlighted the importance of resolving plant seasonal morphological change on river flow dynamics, however, it has remained difficult to resolve both plant morphological detail and motion to date. Through simple extensions of the leaf object model to allow for branching at selected DEM nodes, the approach presented in this study can be further developed for

simulating a wider variety of plant forms, thereby allowing simulations that can capture hydrodynamic changes that occur over the full plant life-cycle.

Acknowledgments, Samples, and Data

This work was supported by the Japan Society for the Promotion of Science under grant 18H01545 and 18KK0119. MRH received funding from LP130100756. The executable binary (windows, mac, linux) of the three-dimensional hydrodynamic model, Fantom, used in this study, is available from http://www.comp.tmu.ac.jp/shintani/fantom.html. The model outputs are available from https://github.com/kuaqua/WRR2019.

References

Abdelrhman, M.A. (2007). Modeling coupling between eelgrass Zostera marina and water flow, Marine Ecology Progress Series. 338, 81-96.

Abdolahpour, M., Ghisalberti, M., McMahon, K., and Lavery, P.S. (2018). The impact of flexibility on flow, turbulence, and vertical mixing in coastal canopies. Limnology and Oceanography. 63, 2777-2792.

Adams, P.A., Hovey, R.K, Hipsey, M.R., Bruce, L.C., Ghisalberti, M., Lowe, R.J., Gruber, R.K., Ruiz-Montoya, L., Maxwell, P.S., Callaghan, D.P., Kendrick, G.A., and O'Brien, K.R. (2016). Feedback between sediment and light for seagrass: Where is it important? Limnology and Oceanography. 61, 1937-1955.

Adams, P.A., Ghisalberti, M., Lowe, R.J., Callaghan, D.P., Baird, M.E., Infantes, E., and O'Brien, K.R. (2018). Water residence time controls the feedback between seagrass, sediment and light: Implications for restoration. Advances in Water Resources. 117, 14-26, https://doi.org/10.1016/j.advwatres.2018.04.004.

Adiyanti, S., Eyre, B.D., Maher, D.T., Santos, I., Golsby-Smith, L., Mangion, P., and Hipsey, M.R. (2016). Stable isotopes reduce parameter uncertainty of an estuarine carbon cycling model. Environmental Modelling & Software. 79, 233-255.

Anderson B.G., Rutherfurd, I.D., and Western, A.W. (2006). An analysis of the influence of riparian vegetation on the propagation of flood waves. Environmental Modelling & Software. 21, 1290-1296.

Boothroyd, R. J., Hardy, R. J., Warburton, J., & Marjoribanks, T. I. (2016). The importance of accurately representing submerged vegetation morphology in the numerical prediction of complex river flow. Earth Surface Processes and Landforms, 41(4), 567-576.

Bouma, T.J., De Vries, M.B., Low, E., Peralta, G., Tanczos, I.C., and Van de Koppel, J. (2005). Trade-offs related to ecosystem engineering: A case study on stiffness of emerging macrophytes. Ecology. 86(8), 2187-2199.

Busari, A.O., and Li, C.W. (2015). A hydraulic roughness model for submerged flexible vegetation with uncertainty estimation. Journal of Hydro-environment Research. 9, 268-280.

Cai, W.J. (2011). Estuarine and coastal ocean carbon paradox: CO2 sinks or sites of terrestrial carbon incineration?. Journal of Hydro-environment Research. 3, 123-145.

525 Dijkstra, J.T., and Uittenbogaard, R.E. (2010). Modeling the interaction between flow and highly
526 flexible aquatic vegetation. Water Resources Research. 46, W12547.
527 Duarte, C.M., Losada, I.J., Hendriks, I.E., Mazarrasa, I., and Marbà, N. (2013). The role of
528 coastal plant communities for climate change mitigation and adaptation. Nature Climate
529 Change. 3(11), 961.
530 Dutta, D., Write, W., Nakayama, K., and Sugawara, Y. (2013). Design of synthetic impact
531 response functions for flood vulnerability assessment under climate change conditions: Case
532 studies in two selected coastal zones in Australia and Japan. Natural Hazards Review. 14, 52-
533 65.
534 Fragoso, C.R., Marques, D.M.L.M., Ferreira, T.F., Janse, J.H., and Nes, E.H. (2011). Potential
535 effects of climate change and eutrophication on a large subtropical shallow lake. Environmental
536 Modelling & Software. 26, 1337-1348.
537 Gac, J. (2014). A large eddy based lattice-Boltzmann simulation of velocity distribution in an
538 open channel flow with rigid and flexible vegetation. Acta Geophysica, 62(1), 180-198.
539 Ghisalberti, M., and Nepf, H. (2006). The structure of the shear layer in flows over rigid and
540 flexible canopies. Environmental Fluid Mechanics. 6(3), 277-301, doi:10.1007/s10652-006-
541 0002-4.
542 Ghisalberti, M., and Nepf, H. (2009). Shallow flows over a permeable medium: The
543 hydrodynamics of submerged aquatic canopies. Transport in Porous Media. 78, 309-326.
544 Guan, M., and Liang, Q. (2017). A two-dimensional hydro-morphological model for river
545 hydraulics and morphology with vegetation. Environmental Modelling & Software. 88, 10-21.
546 Hilt, S., Nuñez, A., Marta, M., Bakker, E.S., Blindow, I., Davidson, T.A., Gillefalk, M.,
547 Hansson, L.A., Janse, J.H., Janssen, A.B. and Jeppesen, E. et al. 2018. Response of submerged
548 macrophyte communities to external and internal restoration measures in north temperate
549 shallow lakes. *Frontiers in plant science*, *9*, p.194.
550 Hirabayashi, Y., Mahendran, R., Kirala, S., Konoshima, L., Yamazaki, D., Watanabe, S., Kim,
551 H., and Kanae, S. (2013). Global flood risk under climate change. Nature Climate Change. 3,
552 816-821.
553 Infantes, E., Orfila, A., Simarro, G., Terrados, J., Luhar, M., and Nepf, H. (2012). Effect of a
554 seagrass (*Posidonia oceanica*) meadow on wave propagation. Marine Ecology Progress Series.
555 456, 63-72.

556 IPCC, (2014). *Climate Change 2014: Synthesis Report. Contribution of Working Groups I, II and*
557 *III to the Fifth Assessment Report of the Intergovernmental Panel on Climate Change* [Core
558 Writing Team, R.K. Pachauri and L.A. Meyer (eds.)]. IPCC, Geneva, Switzerland, 151 pp.
559 Kutija, V., and Hong, H.T.M. (1996). A numerical model for assessing the additional resistance
560 to flow vegetation. Journal of Hydraulic Research. 34, 99-114.
561 Lacy, J.R., and Wylie-Echeverria, S. (2011). The influence of current speed and vegetation
562 density on flow structure in two macrotidal eelgrass canopies. Limnology and Oceanography.
563 1, 38-55.
564 Laniak, G.F., Olchin, G., Goodall, J., Voinov, A., Hill, M., Glynn, P., Whelan, G., Geller, G.,
565 Quinn, N., Blind, M., Peckham, S., Reaney, S., Gaber, N., Kennedy, R., and Hughesm, A.
566 (2013). Integrated environmental modeling: A vision and roadmap for the future.
567 Environmental Modelling & Software. 39, 3-23.
568 Lavery, P.S., Mateo, M., Serrano, O., and Rozaimi, M. (2013). Variability in the carbon storage
569 of seagrass habitats and its implications for global estimates of blue carbon ecosystem service.
570 PloS one. 8(9), e73748.
571 Li, Y., Wang, Y., Anim, D.O., Tang, C., Du, W., Ni, L., Yu, Z., and Acharya, K. (2014). Flow
572 characteristics in different densities of submerged flexible vegetation from an open-channel
573 flume study of artificial plants. Geomorphology. 204, 314-324.
574 Luhar, M., Coutu, S., Infantes, E., Fox, S., and Nepf, H. (2010). Wave-induced velocities inside a
575 model seagrass bed. Journal of Geophysical Research. 115, C12005.
576 Luhar, M., Infantes, E., Orfila, A., Terrados, J., and Nepf, H. (2013). Field observations of wave-
577 induced streaming through a submerged seagrass (Posidonia oceanica) meadow. Journal of
578 Geophysical Research. 118, 1955-1968.
579 Luhar, M., and Nepf, H. (2011). Flow-induced reconfiguration of buoyant and flexible aquatic
580 vegetation. Limnology and Oceanography. 56(6), 2003-2017, doi:10.4319/lo.2011.56.6.2003.
581 Luhar, M., and Nepf, H. (2013). From the blade scale to the reach scale: A characterization of
582 aquatic vegetative drag. Advances in Water Resources. 51, 305-316,
583 doi:10.1016/j.advwatres.2012.02.002.
584 Luhar, M., and Nepf, H. (2016). Wave-induced dynamics of flexible blades. Journal of Fluids
585 and Structures. 61, 20-41.

586 Me, W., Hamilton, D.P., McBride, C.G., Abell, J.M., and Hicks, B.J. (2018). Modelling
587 hydrology and water quality in a mixed land use catchment and eutrophic lake: Effects of
588 nutrient load reductions and climate change. Environmental Modelling & Software. 109, 114–
589 133.
590 Marjoribanks, T. I., Hardy, R. J., Lane, S. N., & Parsons, D. R. (2014). High-resolution
591 numerical modelling of flow-vegetation interactions. Journal of Hydraulic Research, 52(6),
592 775-793.
593 Murphy, E., Ghisalberti, M., and Nepf, H. (2007). Model and laboratory study of dispersion in
594 flows with submerged vegetation. Water Resources Research. 43, W05438.
595 sea level rise. Hydrological Research Letters 7, 1-5.
596 Nakayama, K. (2006). Comparisons of CIP, compact and CIP-CSL2 schemes for reproducing
597 internal solitary waves. International Journal for Numerical Methods in Fluids. 51, 197-219.
598 Nakayama, K., and Imberger, J. (2010). Residual circulation due to internal waves shoaling on a
599 slope. Limnology and Oceanography. 55, 1009-1023.
600 Nakayama, K., Nguyen, H.D., Shintani, T., and Komai, K. (2016). Reversal of secondary
601 circulations in a sharp channel bend. Coastal Engineering Journal. 58, 1650002.
602 Nakayama, K., Shintani, T., Kokubo, K., Kakinuma, T., Maruya, Y., Komai, K., and Okada, T.
603 (2012). Residual current over a uniform slope due to breaking of internal waves in a two-layer
604 system. Journal of Geophysical Research. 117, C10002, 11.
605 Nakayama, K., Shintani, T., Shimizu, K., Okada, T., Hinata, H., and Komai, K. (2014).
606 Horizontal and residual circulations driven by wind stress curl in Tokyo Bay. Journal of
607 Geophysical Research. 119, 1977-1992.
608 Nakayama, K., Sivapalan, M., Sato, C., and Furukawa, K. (2010). Stochastic characterization of
609 the onset of and recovery from hypoxia in Tokyo Bay, Japan: Derived distribution analysis
610 based on “strong wind” events. Water Resources Research. 46, W12532.
611 Nakayama, K., Sato, T., Shimizu, K., and Boegman, L. (2019). Classification of internal solitary
612 wave breaking over a slope. Physical Review Fluids. 4, 014801.
613 Noarayanan, L., Murali, K., and Sundar, V. (2012). Manning’s ‘n’ co-efficient for flexible
614 emergent vegetation in tandem configuration. Journal of Hydro-environment Research. 6, 51-
615 62.

Nellemann, C., Corcoran, E., Duarte, C.M., Valdés, L., De Young, C., Fonseca, L., and Grimsditch, G., (Eds.) (2009). Blue carbon. A rapid response assessment. United Nations Environmental Programme. GRID-Arendal. Norway.

Nepf, H.M. (2012). Flow and transport in regions with aquatic vegetation. Annual Review of Fluid Mechanics. 44, 123-142.

Prentice, C., Lewis, M.H., Smith, R.S., and Salomon, A.K. (2019). Reduced water motion enhances organic carbon stocks in temperate eelgrass meadows. Limnology and Oceanography. 9999, 1-16.

Sachse, R., Petzoldt, T., Blumstock, M., Moreira, S., Pätzig, M., Rücker, J., Janse, J.H., Mooij, W.M., and Hilt, S. (2014). Extending one-dimensional models for deep lakes to simulate the impact of submerged macrophytes on water quality. Environmental Modelling & Software. 61, 410−423.

Seginer, I., Mulhearn, P.J., Bradely, E.F., and Finnigan, J.J. (1976). Turbulent flow in a model plant canopy. Boundary-Layer Meteorologyogy. 10, 423-453.

Song, X.P., Hansen, M.C., Stehman, S.V., Potapov, P.V., Tyukavina, A., Vermote, E.F., and Townshend, J.R. (2018). Global land change from 1982 to 2016. Nature. 1-5.

Stoesser, T., Wilson, C.A.M.E., Bates, P.D., and Dittrich, A. (2003). Application of a 3D numerical model to a river with vegetated floodplains. Journal of Hydroinformatics. 5(2), 99-112.

Suzuki, T., Zijlema, M., Burger, B., Meijer, M.C., and Narayan, S. (2011). Wave dissipation by vegetation with layer schematization in SWAN, Coastal Engineering. 59, 64-71.

Tezuka, S., Takiguchi, H., Kazama, S., Sarukkalige, R., Sato, A., and Kawagoe, S. (2013). Estimation of the effects of climate change on flood-triggered economic losses in Japan. Natural Hazards and Earth System Sciences. 1, 1619-1649.

Thomas, F.I.M., Cornelisen, C.D., and Zande, J.M. (2000). Effects of water velocity and canopy morphology on ammonium uptake by seagrass communities. Ecology. 81(10), 2704-2713.

Thuiller, W. (2007). Biodiversity: Climate change and the ecologist. Nature. 448, 550–552.

Trolle, D., Elliott, J.A., Mooij, W.M., Janse, J.H., Bolding, K., Hamilton, D.P., and Jeppesen, E. (2014). Advancing projections of phytoplankton responses to climate change through ensemble modellingq. Environmental Modelling & Software. 61, 371-379.

646 Turuncoglu, U.U., Dalfes, N., Murphy, S., and DeLuca, C. (2013). Toward self-describing and
647 workflow integrated Earth system models: A coupled atmosphere-ocean modeling system
648 applicationq. Environmental Modelling & Software. 39, 247-262.
649 Umlauf, L., and Burchard, H. (2003). A generic length-scale equation for geophysical turbulence
650 models. Journal of Marine Research. 61, 235-265.
651 Verduin, J.J., and Backhaus, J.O. (2000). Dynamics of plant-flow interactions for the seagrass
652 Amphibolis antarctica: field observations and model simulations. Estuarine, Coastal and Shelf
653 Science. 50, 185-204.
654 Vilas, M.P., Marti, C.L., Adams, M.P., Oldham, C.E., and Hipsey, M.R. (2017). Invasive
655 macrophytes control the spatial and temporal patterns of temperature and dissolved oxygen in a
656 shallow lake: A proposed feedback mechanism of macrophyte loss. Frontiers in Plant Science.
657 8, 2097.
658 Warner, J.C., Sherwood, C.R., Arango, H.G., and Signell, R.P. (2005). Performance of four
659 turbulence closure models implemented using a generic length scale method. Ocean Modelling.
660 8, 81-113.
661 Weitzman, J.S., Aveni-Deforge, K., Koseff, J.R., and Thomas, F.I.M. (2013). Uptake of issolved
662 inorganic nitrogen by shallow seagrass communities exposed to wave-driven unsteady flow.
663 Marine Ecology Progress Series. 475, 65-83.
664 Weitzman, J.S., Zeller, R.B., Thomas, F.I.M., and Koseff, J.R. (2015). The attenuation of
665 current - and wave - driven flow within submerged multispecific vegetative canopies.
666 Limnology and Oceanography. 60, 1855-1874.
667 Whittaker, P., Wilson, C.A.M.E., and Aberle, J. (2015). An improved Cauchy number approach
668 for predicting the drag and reconfiguration of flexible vegetation. Advances in Water
669 Resources. 83, 28-35.
670 Wilson, C.A.M.E., Yagci, O., Rauch, H.P., and Olsen, N.R.B. (2006). 3D numerical modelling of
671 a willow vegetated river/floodplain system. Journal of Hydrology. 327, 13-21.
672 Wilson, C.A.M.E. (2007). Flow resistance models for flexible submerged vegetation. Journal of
673 Hydrology. 342, 213-222.
674 Zeller, R.B., Weitzman, J.S., Abbett, M.E., Zarama, F.J., Fringer, O.B., and Koseff, J.R. (2014).
675 Improved parameterization of seagrass blade dynamics and wave attenuation based on
676 numerical and laboratory experiments. Limnology and Oceanography. 59, 251-266.

677 **Figures**

678

679 Figure 1 Schematic diagram of SAV model

680

681 Figure 2 Flow chart of SAV model. N denotes the number of CPU for wave-current parallel
682 computations, and M denotes the number of CPU for seagrass (seagrass) parallel computations.

683

684 Figure 3 Laboratory experiment setup in an open channel. Velocity was measured at 2 points
685 using an acoustic doppler current meter. Real seagrass was obtained in the eastern part of
686 Hokkaido Island.

687

688 Figure 4 Evaluation of SAV model for four cases, cases 1 to 4. (a) Definition of positions of
689 every 0.2 m from the root to the top of seagrass. (b) Comparisons of horizontal position between
690 laboratory experiments and numerical computations. (c) Comparisons of vertical position
691 between laboratory experiments and numerical computations.

692

693 Figure 5 Evaluation of SAV model by using velocities under a uniform current for four cases,
694 cases 1 to 4. Black and white squares denote laboratory experiments and numerical
695 computations, respectively. “no.1” and “no.2” corresponds to the front and behind of seagrass
696 meadow.

697

698 Figure 6 Comparisons with laboratory experiments. Green lines indicate seagrasses from
699 computations. Contours show horizontal velocity. (a) case Lab1 that corresponds to case 1. (b)
700 case ES. (c) case EL. (d) case CdS. (e) case CdL. (f) case fcS. (g) case fcL.

701

702 Figure 7 Contribution of elastic modulus, drag, friction, lift forces and buoyancy to momentum
703 equations obtained from SAV model for case Lab1. Horizontal acceleration due to drag, friction
704 and *EI* (a) at the front seagrass, (b) at the middle seagrass, and (c) at the most behind seagrass,
705 respectively. Vertical acceleration due to drag, friction, lift and buoyancy (d) at the front
706 seagrass, (e) at the middle seagrass, and (f) at the most behind seagrass, respectively.

707

Figure 8 Seagrass and horizontal velocity of case w15v10d_L. Green lines indicate seagrasses from computations. Contours show horizontal velocity.

Figure 9 Deflected vegetation height for case C. (a) cases w05v05d_L to w05v10d_S with the water depth of 0.5 m. (b) cases w10v05d_L to w10v10d_S with the water depth of 1.0 m. (c) cases w15v05d_L to w15v10d_S with the water depth of 1.5 m.

Figure 10 Vertically mean horizontal velocities inside of and above seagrass. (a) cases w05v05d_L to w05v10d_S with the water depth of 0.5 m. (b) cases w10v05d_L to w10v10d_S with the water depth of 1.0 m. (c) cases w15v05d_L to w15v10d_S with the water depth of 1.5 m.

Figure 11 Friction coefficient. (a) cases w05v10d_L to w05v10d_S with the water depth of 0.5 m. (b) cases w10v05d_L to w10v10d_S with the water depth of 1.0 m. (c) cases w15v05d_L to w15v10d_S with the water depth of 1.5 m. (d) Vertical profile of horizontal velocity at the distance of 3 m from the seagrass front in cases w15v05d_L to w15v05d_S. (e) Vertical profile of horizontal velocity at the distance of 3 m from the seagrass front in cases w15v10d_L to w15v10d_S.

Figure 12 Computation with and without seagrass motion by using case w15v05d_L conditions. (a) Seagrass and horizontal velocity of case w15v05d_L without seagrass motion. Contours show horizontal velocity. (b) Difference of horizontal velocity with – without seagrass motion in case w15v05d_L. (c) Friction coefficient with and without seagrass motion.

Tables

Table I Conditions for Laboratory experiments.

Table II Computational conditions. Case Lab1 corresponds to case 1. Capital letters of case names, “E”, “Cd”, “fc, and “Cl”, denote elastic modulus, drag coefficient, friction coefficient, and lift force coefficient. Subscripts, “S” and “L”, denote smaller and larger values of “E”, “Cd”, “fc, and “Cl”.

Table III Computational conditions for investigating velocity, deflected vegetation height and friction coefficient. Seagrass length is 1 m with 600 shoots. “w” and the following number mean water depth, and “v” and the following number mean velocity. For example, “w05v02” means the water depth of 0.5 m and the velocity of 0.5 m s-1. “d” denotes density of seagrass, and Subscripts, “S” and “L”, denote smaller and larger values of density of seagrass.

747 Table I Conditions for Laboratory experiments.

case	leaf brade length (m)	uniform current (m s^{-1})
1	1.0	0.08
2	1.0	0.04
3	0.35	0.08
4	0.35	0.04

748 The condition of flow is uniform, and water depth is 0.7 m.
749
750

751 Table II Computational conditions. Case Lab1 corresponds to case 1. Capital letters of case names, "E", "Cd", "fc,
752 and "Cl", denote elastic modulus, drag coefficient, friction coefficient, and lift force coefficient. Subscripts, "S" and
753 "L", denote smaller and larger values of "E", "Cd", "fc, and "Cl".

case	***EI* (N m^2)**	***E* (GPa)**	C_D	f_c	*Cl*
Lab1	1.1×10^{-3} to 4.1×10^{-3}	1.3 to 5.0	1.0	0.30	0.10
E_S	0.8×10^{-3} to 3.1×10^{-3}	1.0 to 3.7	1.0	0.30	0.10
E_L	1.3×10^{-3} to 5.2×10^{-3}	1.6 to 6.2	1.0	0.30	0.10
Cd_S	1.1×10^{-3} to 4.1×10^{-3}	1.3 to 5.0	0.5	0.30	0.10
Cd_L	1.1×10^{-3} to 4.1×10^{-3}	1.3 to 5.0	2.0	0.30	0.10
fc_S	1.1×10^{-3} to 4.1×10^{-3}	1.3 to 5.0	1.0	0.15	0.10
fc_L	1.1×10^{-3} to 4.1×10^{-3}	1.3 to 5.0	1.0	0.60	0.10
Cl_S	1.1×10^{-3} to 4.1×10^{-3}	1.3 to 5.0	1.0	0.30	0.05
Cl_L	1.1×10^{-3} to 4.1×10^{-3}	1.3 to 5.0	1.0	0.30	0.20

754 The condition of flow is uniform, and water depth is 0.7 m.
755

Table III Computational conditions for investigating velocity, deflected vegetation height and friction coefficient. Seagrass length is 1 m with 600 shoots. "w" and the following number mean water depth, and "v" and the following number mean velocity. For example, "w05v02" means the water depth of 0.5 m and the velocity of 0.5 m s^{-1}. "d" denotes density of seagrass, and Subscripts, "S" and "L", denote smaller and larger values of density of seagrass.

case	**water depth (m)**	**velocity (m s^{-1})**	**density of seagrass (shoot m^{-2})**
$w05v05d_L$	0.5	0.05	100
$w05v05d_S$	0.5	0.05	44
$w05v10d_L$	0.5	0.10	100
$w05v10d_S$	0.5	0.10	44
$w10v05d_L$	1.0	0.05	100
$w10v05d_S$	1.0	0.05	44
$w10v10d_L$	1.0	0.10	100
$w10v10d_S$	1.0	0.10	44
$w15v05d_L$	1.5	0.05	100
$w15v05d_S$	1.5	0.05	44
$w15v10d_L$	1.5	0.10	100
$w15v10d_S$	1.5	0.10	44

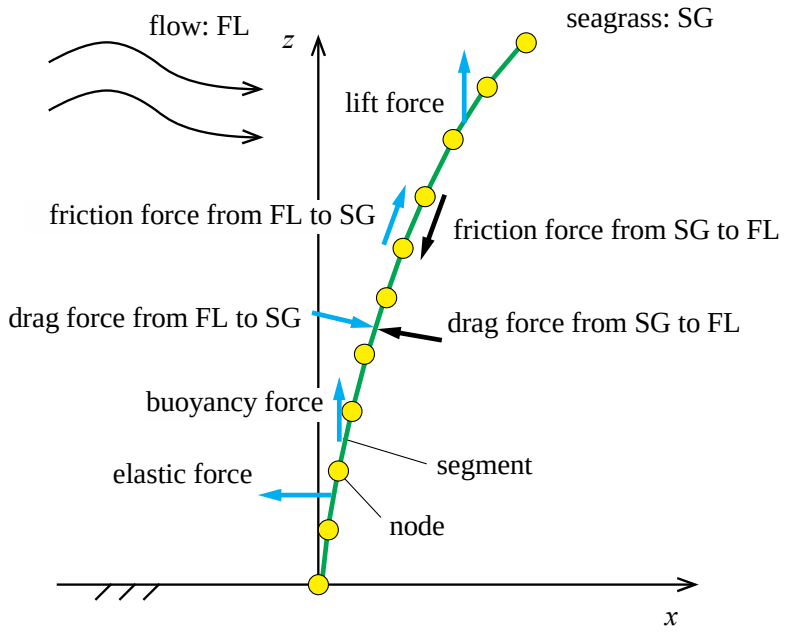

Figure 1 Schematic diagram of SAV model

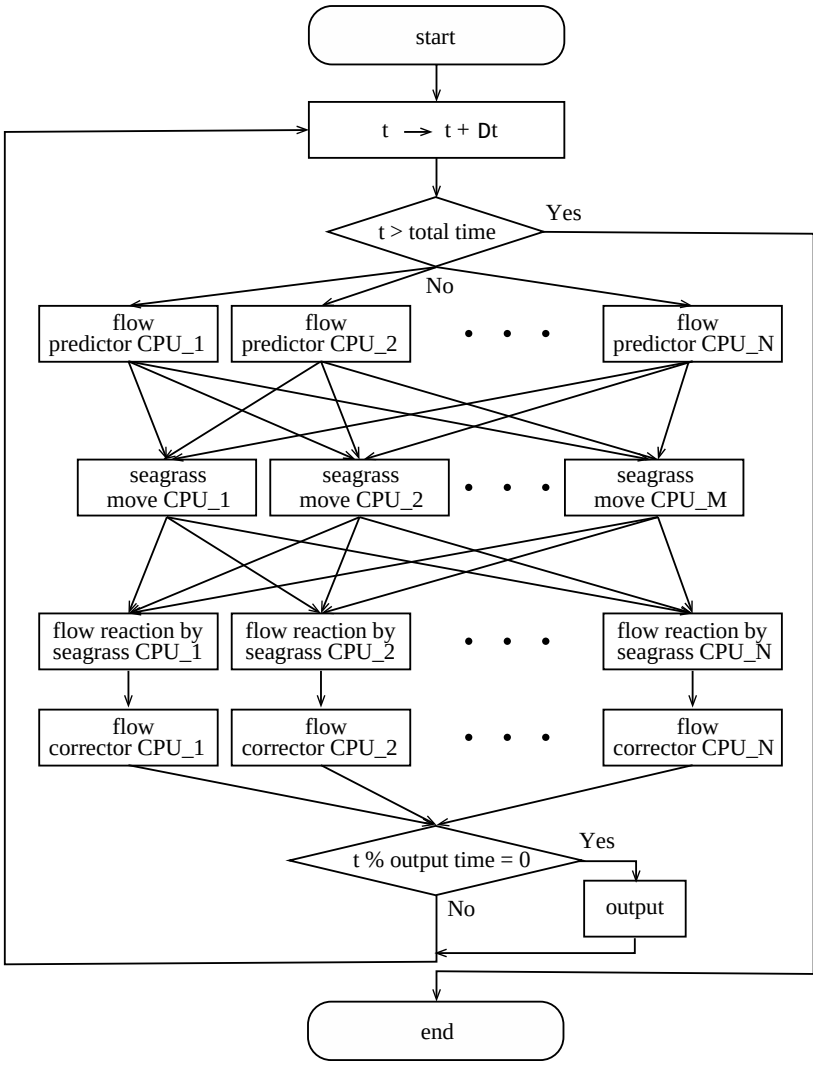

Figure 2 Flow chart of SAV model. N denotes the number of CPU for wave-current parallel computations, and M denotes the number of CPU for seagrass (seagrass) parallel computations.

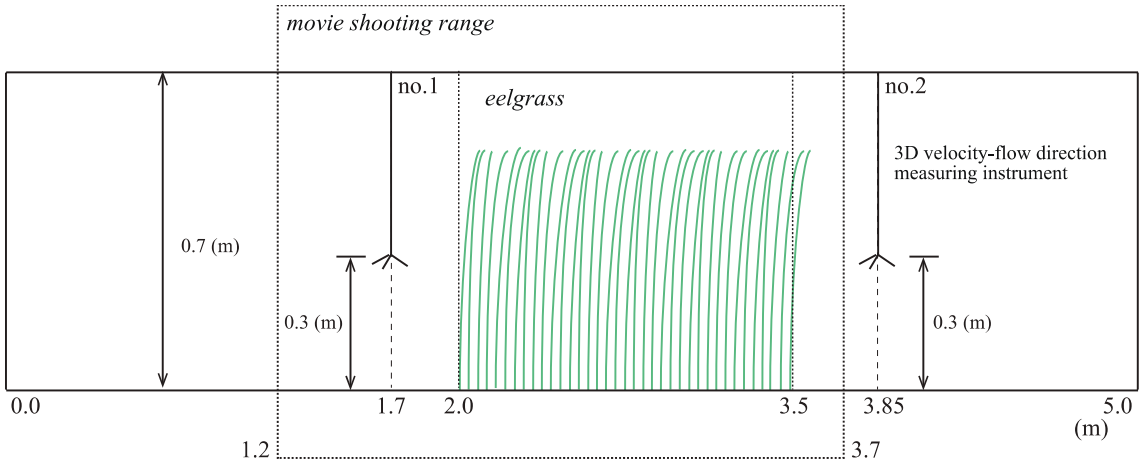

Figure 3 Laboratory experiment setup in an open channel. Velocity was measured at 2 points using an acoustic doppler current meter. Real seagrass was obtained in the eastern part of Hokkaido Island.

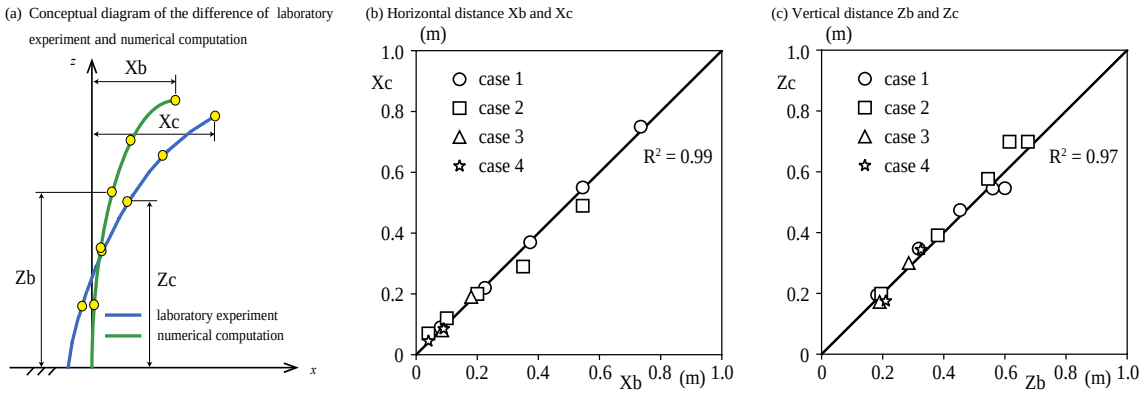

Figure 4 Evaluation of SAV model for four cases, cases 1 to 4. (a) Definition of positions of every 0.2 m from the root to the top of seagrass. (b) Comparisons of horizontal position between laboratory experiments and numerical computations. (c) Comparisons of vertical position between laboratory experiments and numerical computations.

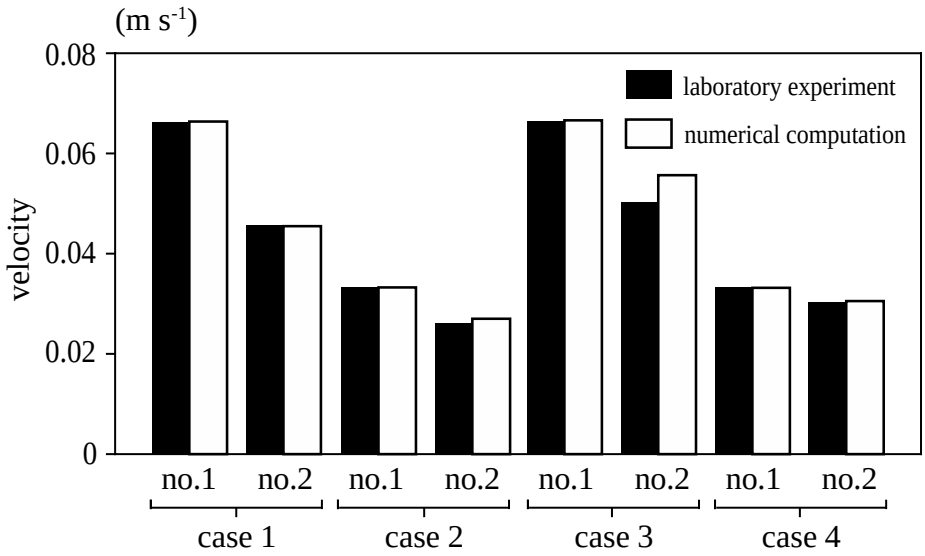

Figure 5 Evaluation of SAV model by using velocities under a uniform current for four cases, cases 1 to 4. Black and white squares denote laboratory experiments and numerical computations, respectively. “no.1” and “no.2” corresponds to the front and behind of seagrass meadow.

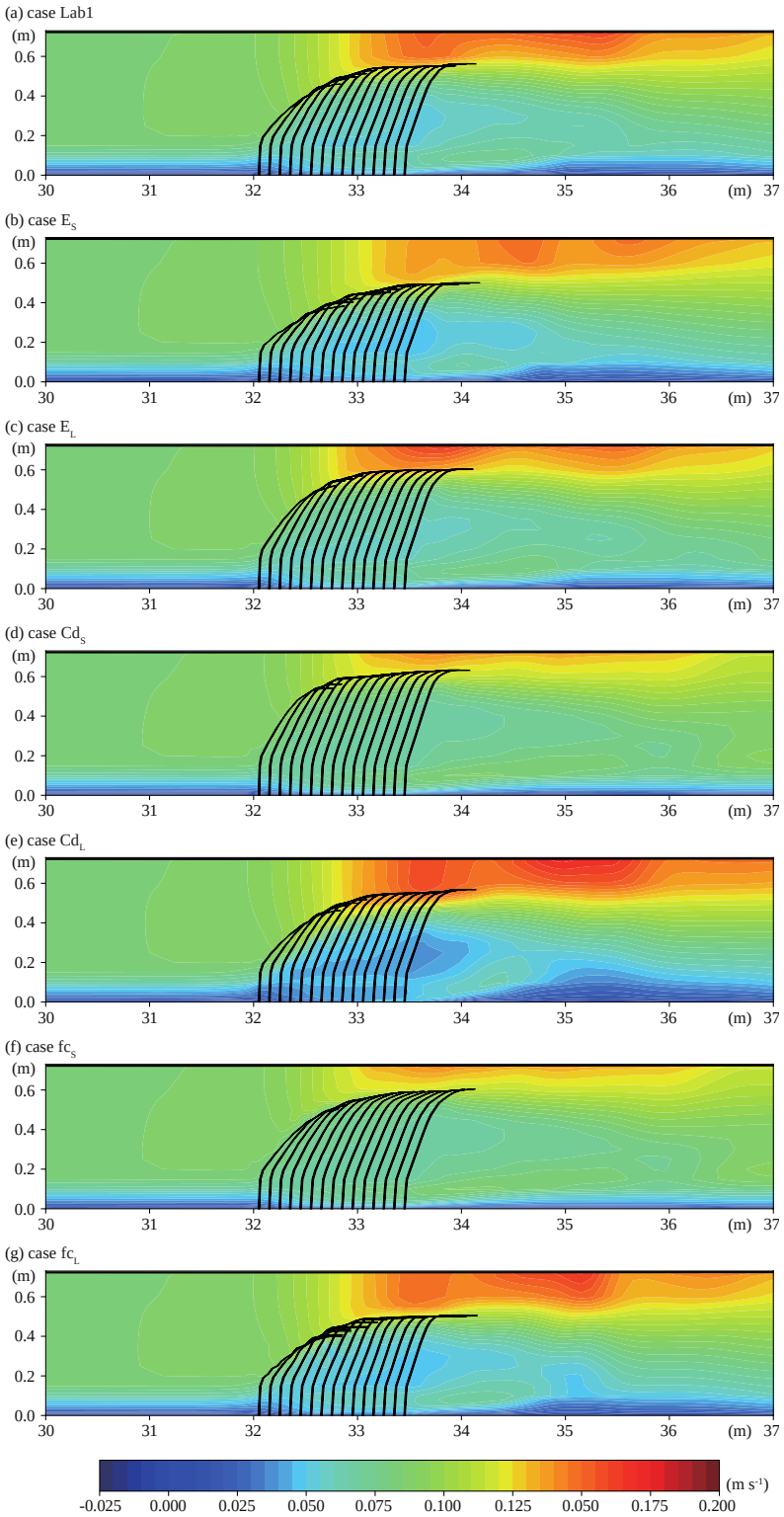

Figure 6 Comparisons with laboratory experiments. Green lines indicate seagrasses from computations. Contours show horizontal velocity. (a) case Lab1 that corresponds to case 1. (b) case E_S. (c) case E_L. (d) case Cd_S. (e) case Cd_L. (f) case fc_S. (g) case fc_L.

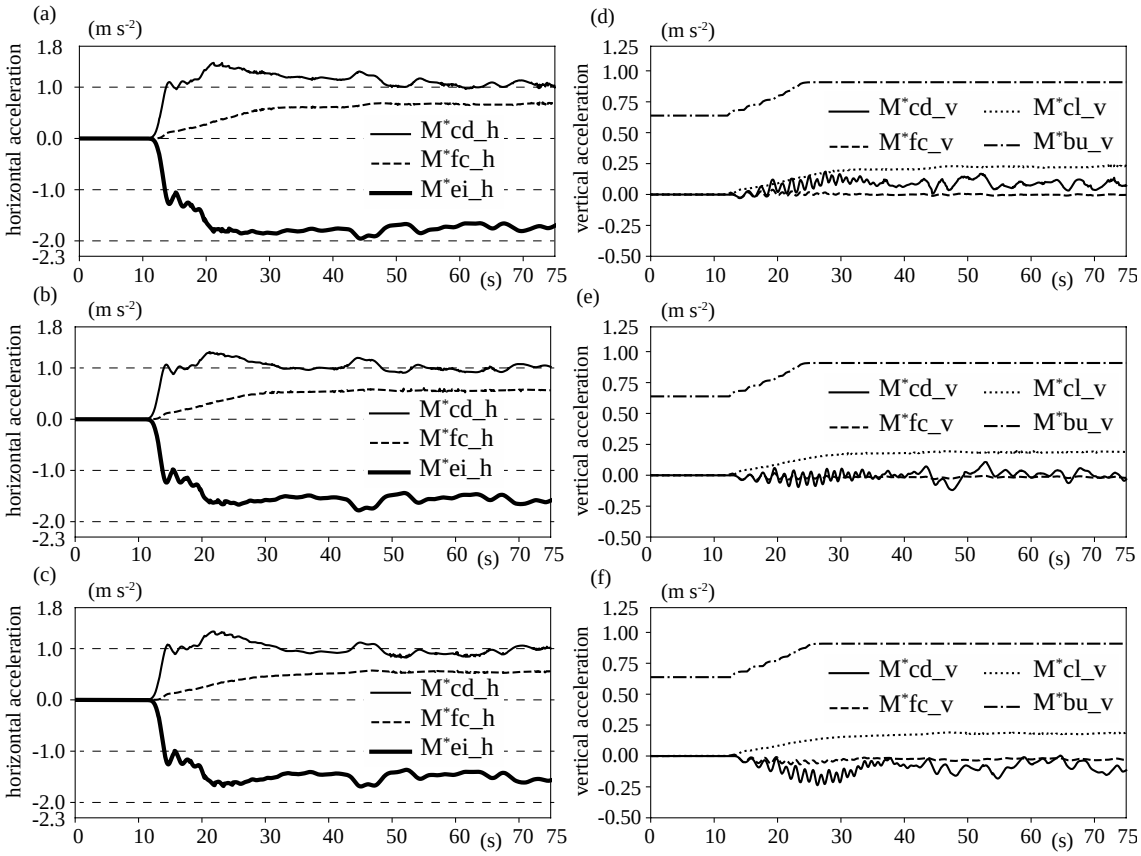

Figure 7 Contribution of elastic modulus, drag, friction, lift forces and buoyancy to momentum equations obtained from SAV model for case Lab1. Horizontal acceleration due to drag, friction and *EI* (a) at the front seagrass, (b) at the middle seagrass, and (c) at the most behind seagrass, respectively. Vertical acceleration due to drag, friction, lift and buoyancy (d) at the front seagrass, (e) at the middle seagrass, and (f) at the most behind seagrass, respectively.

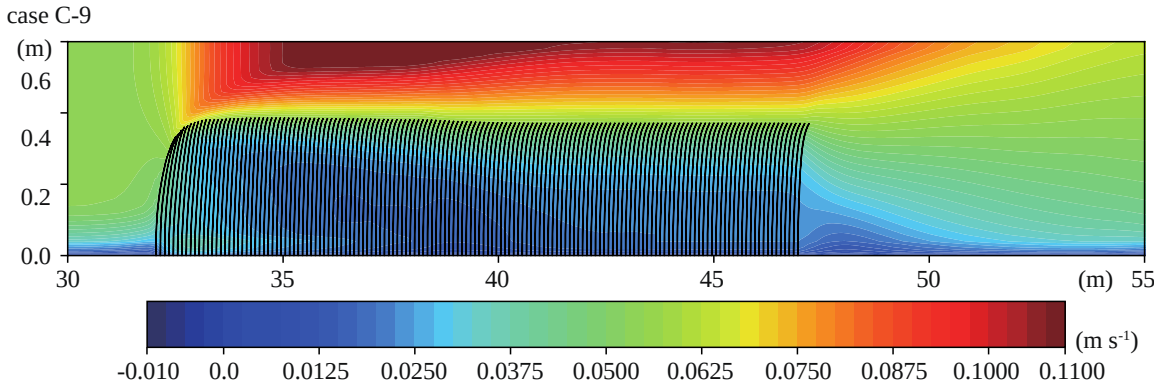

Figure 8 Seagrass and horizontal velocity of case w15v10d_L. Green lines indicate seagrasses from computations. Contours show horizontal velocity.

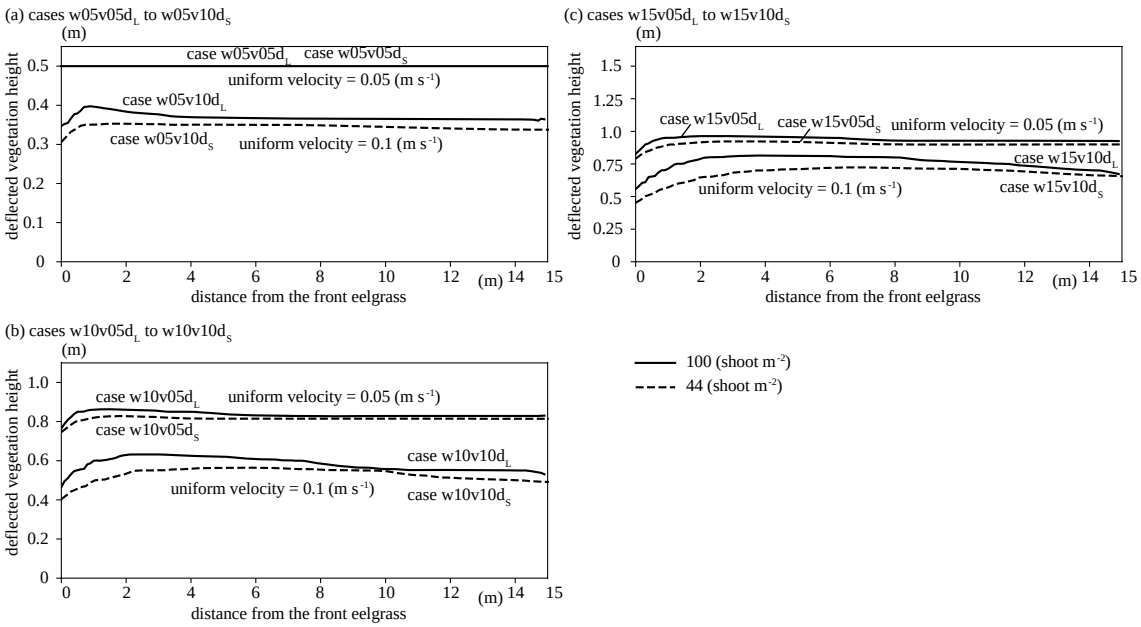

Figure 9 Deflected vegetation height for case C. (a) cases w05v05d$_L$ to w05v10d$_S$ with the water depth of 0.5 m. (b) cases w10v05d$_L$ to w10v10d$_S$ with the water depth of 1.0 m. (c) cases w15v05d$_L$ to w15v10d$_S$ with the water depth of 1.5 m.

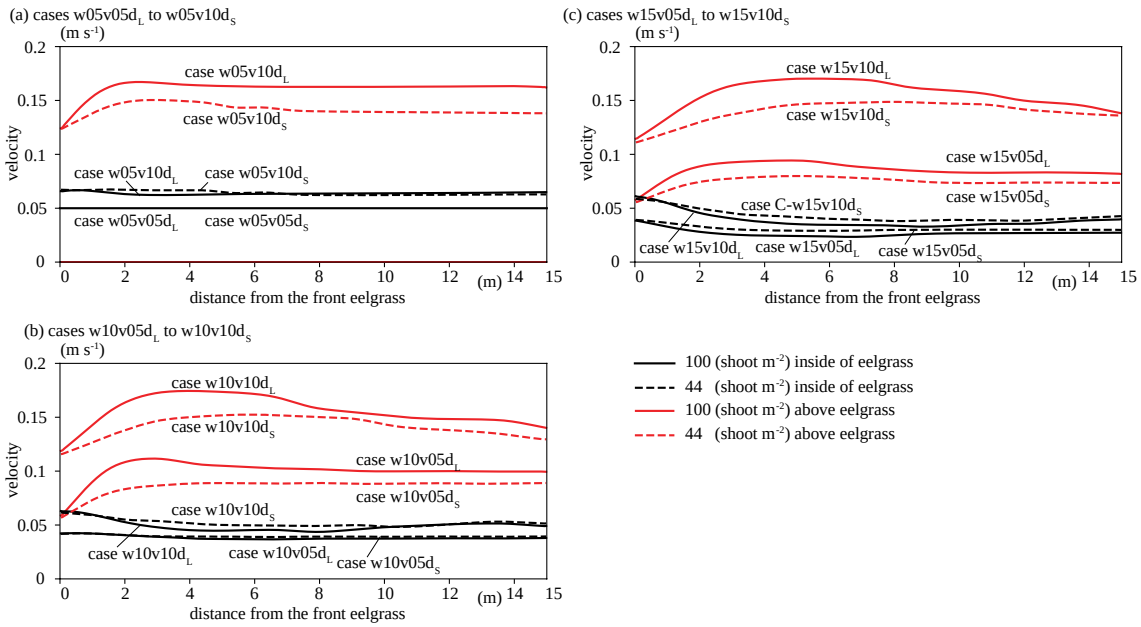

Figure 10 Vertically mean horizontal velocities inside of and above seagrass. (a) cases w05v05d$_L$ to w05v10d$_S$ with the water depth of 0.5 m. (b) cases w10v05d$_L$ to w10v10d$_S$ with the water depth of 1.0 m. (c) cases w15v05d$_L$ to w15v10d$_S$ with the water depth of 1.5 m.

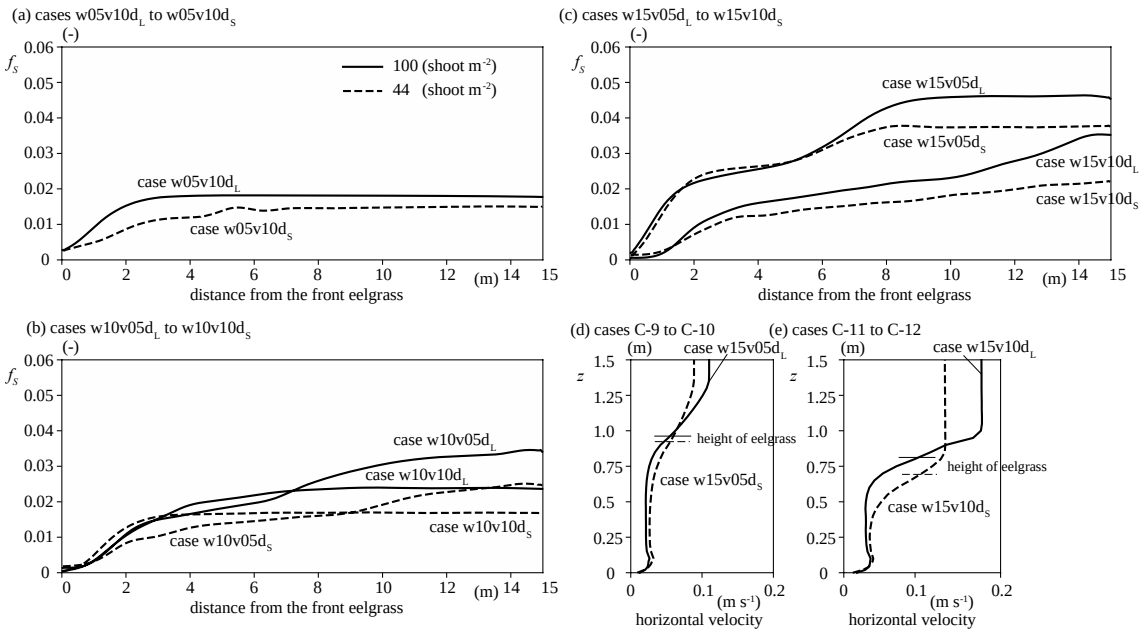

Figure 11 Friction coefficient. (a) cases $w05v10d_L$ to $w05v10d_S$ with the water depth of 0.5 m. (b) cases $w10v05d_L$ to $w10v10d_S$ with the water depth of 1.0 m. (c) cases $w15v05d_L$ to $w15v10d_S$ with the water depth of 1.5 m. (d) Vertical profile of horizontal velocity at the distance of 3 m from the seagrass front in cases $w15v05d_L$ to $w15v05d_S$. (e) Vertical profile of horizontal velocity at the distance of 3 m from the seagrass front in cases $w15v10d_L$ to $w15v10d_S$.

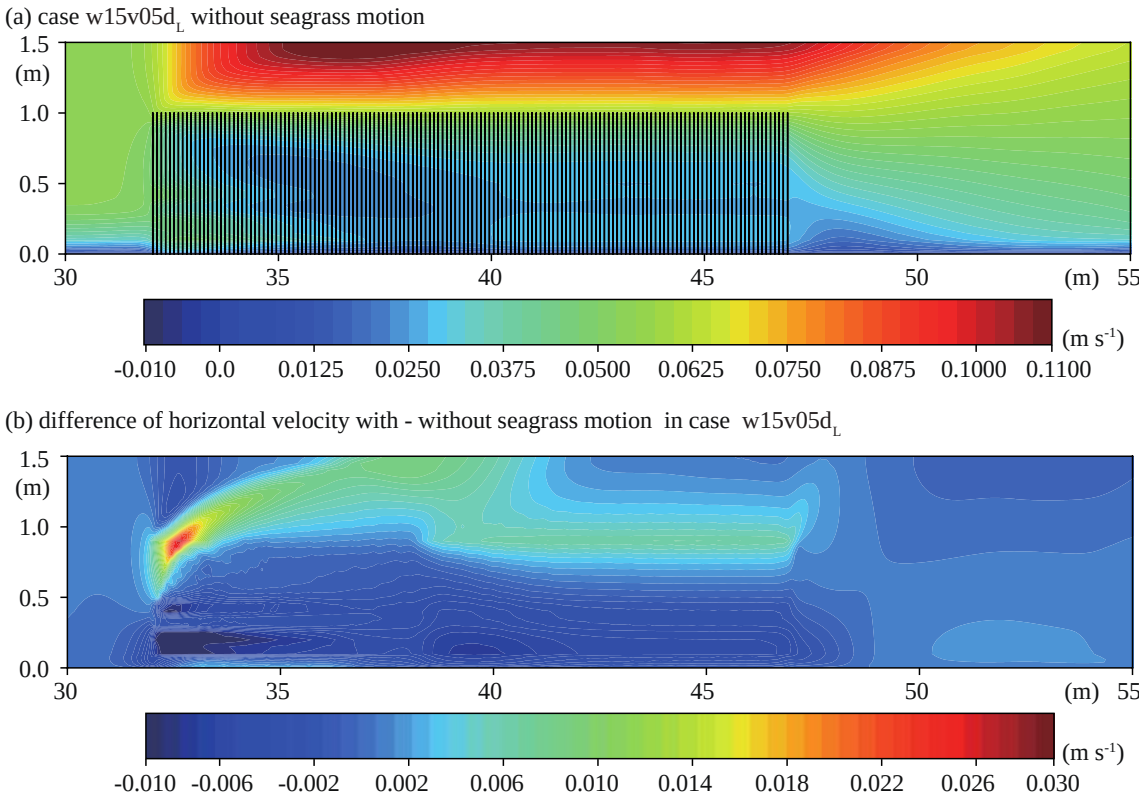

Figure 12 Computation with and without seagrass motion by using case w15v05d$_L$ conditions. (a) Seagrass and horizontal velocity of case w15v05d$_L$ without seagrass motion. Contours show horizontal velocity. (b) Difference of horizontal velocity with – without seagrass motion in case w15v05d$_L$. (c) Friction coefficient with and without seagrass motion.

Figure 1.

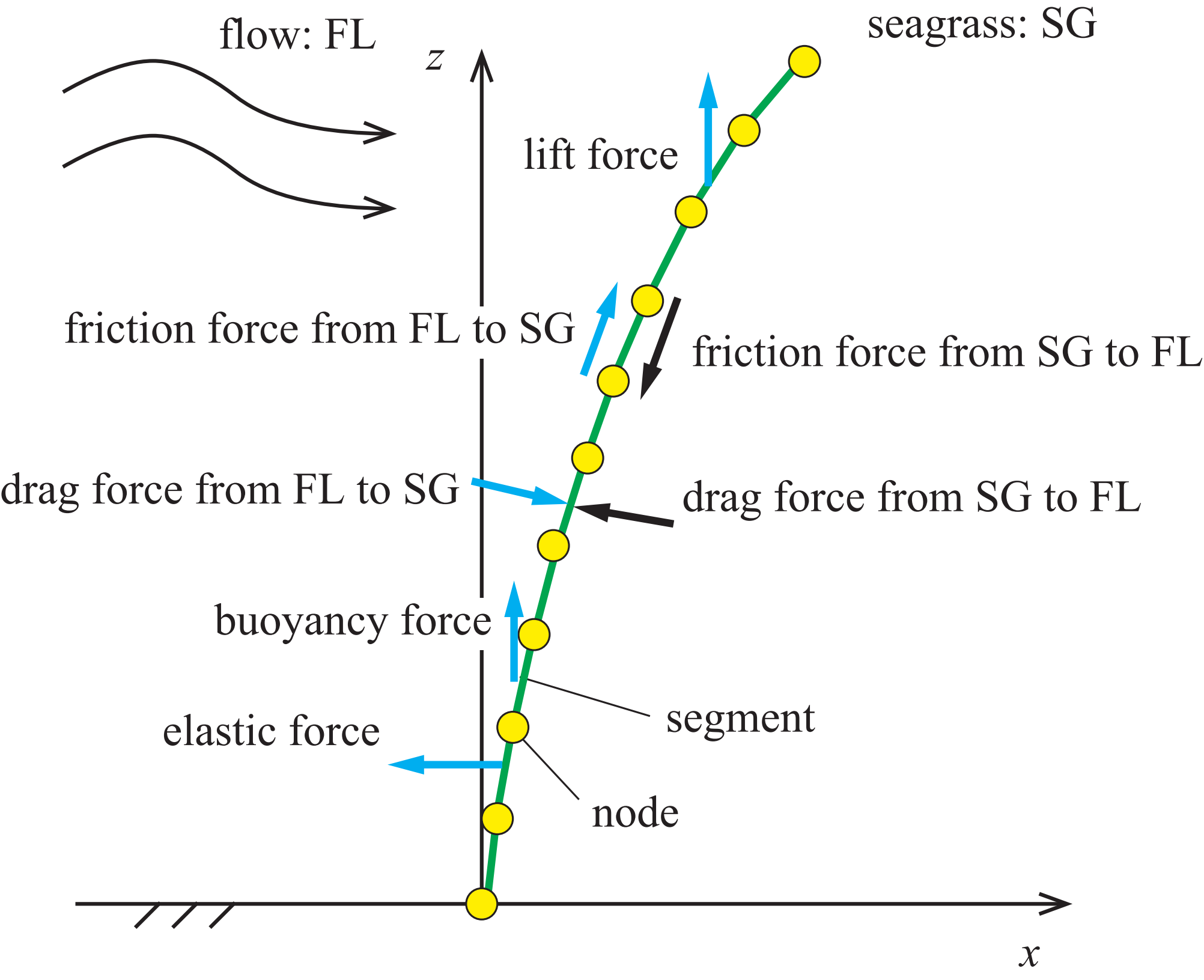
flow: FL
seagrass: SG
z
lift force
friction force from FL to SG
friction force from SG to FL
drag force from FL to SG
drag force from SG to FL
buoyancy force
segment
elastic force
node
x

Figure 2.

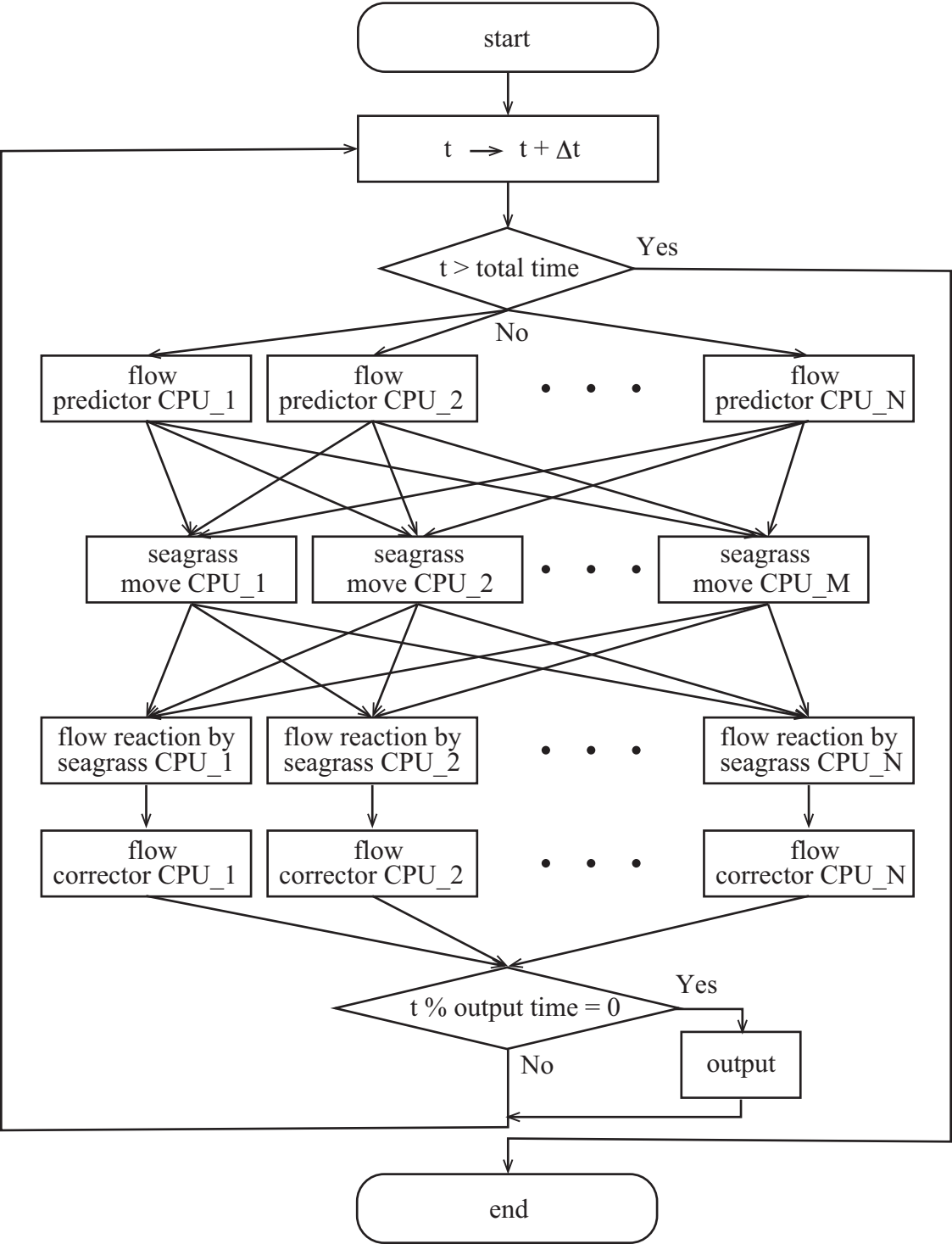
start
t → t + Δt
t > total time
Yes
No
flow predictor CPU_1
flow predictor CPU_2
flow predictor CPU_N
seagrass move CPU_1
seagrass move CPU_2
seagrass move CPU_M
flow reaction by seagrass CPU_1
flow reaction by seagrass CPU_2
flow reaction by seagrass CPU_N
flow corrector CPU_1
flow corrector CPU_2
flow corrector CPU_N
t % output time = 0
Yes
No
output
end

Figure 3.

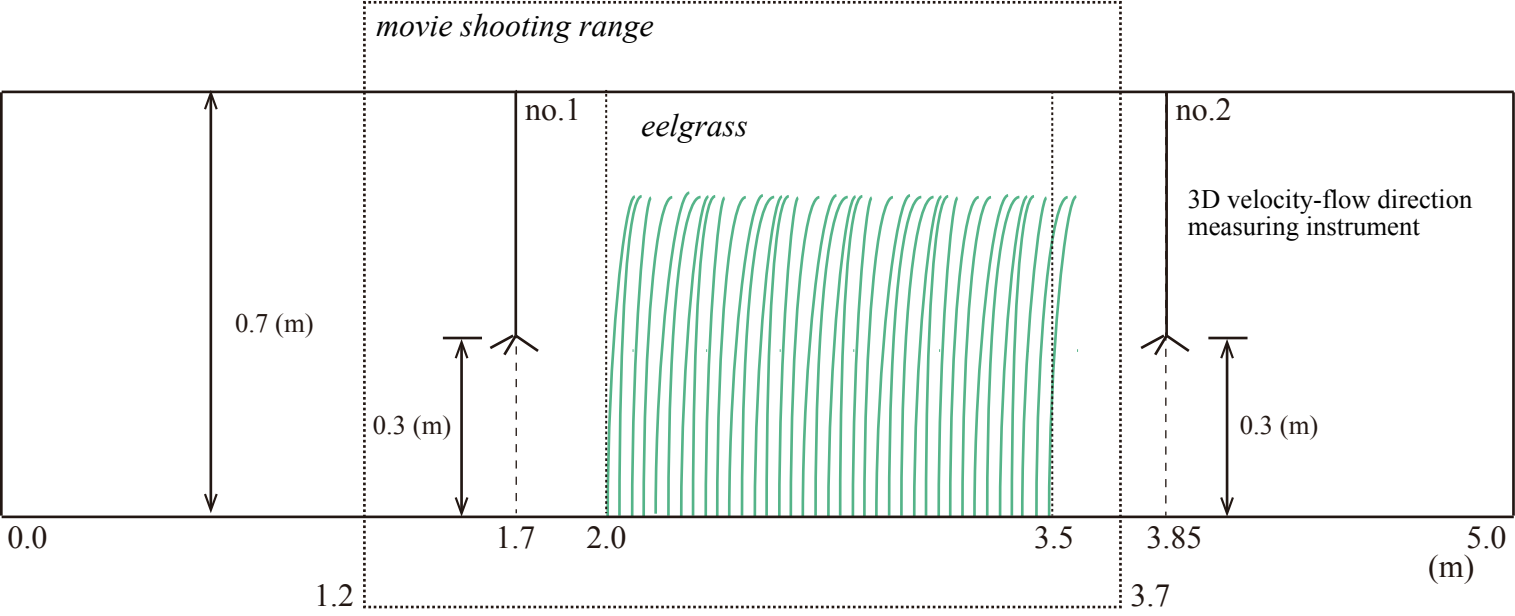
movie shooting range
no.1
eelgrass
no.2
3D velocity-flow direction
measuring instrument
0.7 (m)
0.3 (m)
0.3 (m)
0.0
1.7
2.0
3.5
3.85
5.0
(m)
1.2
3.7

Figure 4.

(a) Conceptual diagram of the difference of laboratory experiment and numerical computation

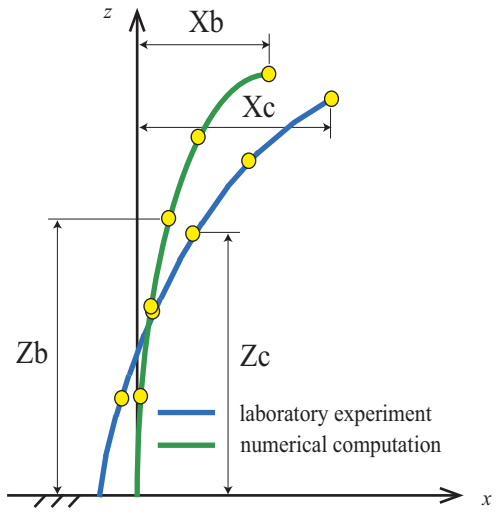

(b) Horizontal distance Xb and Xc

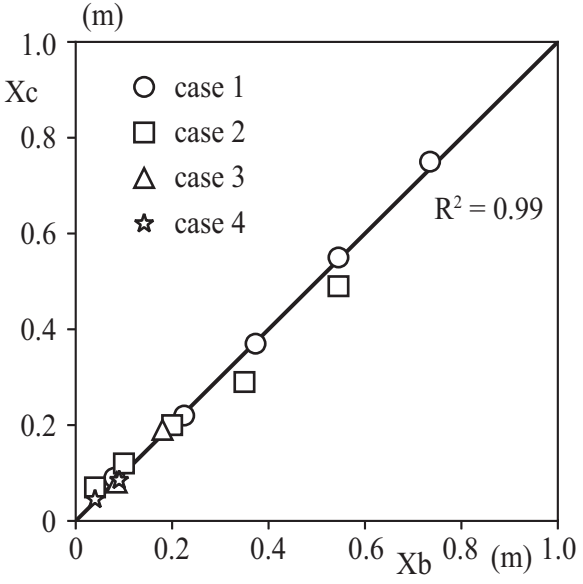

(c) Vertical distance Zb and Zc

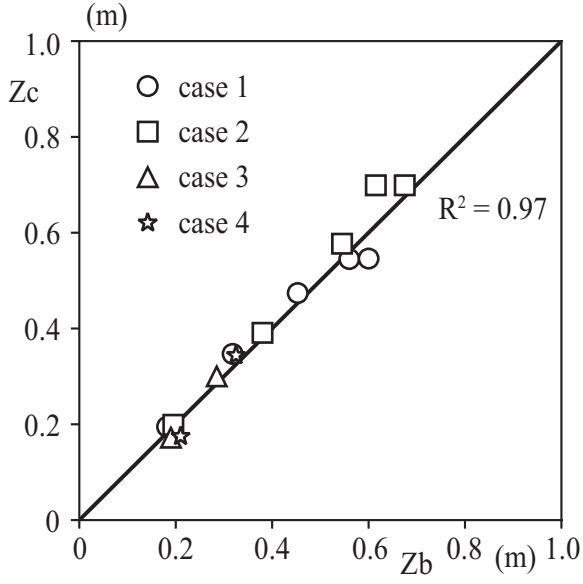

Figure 5.

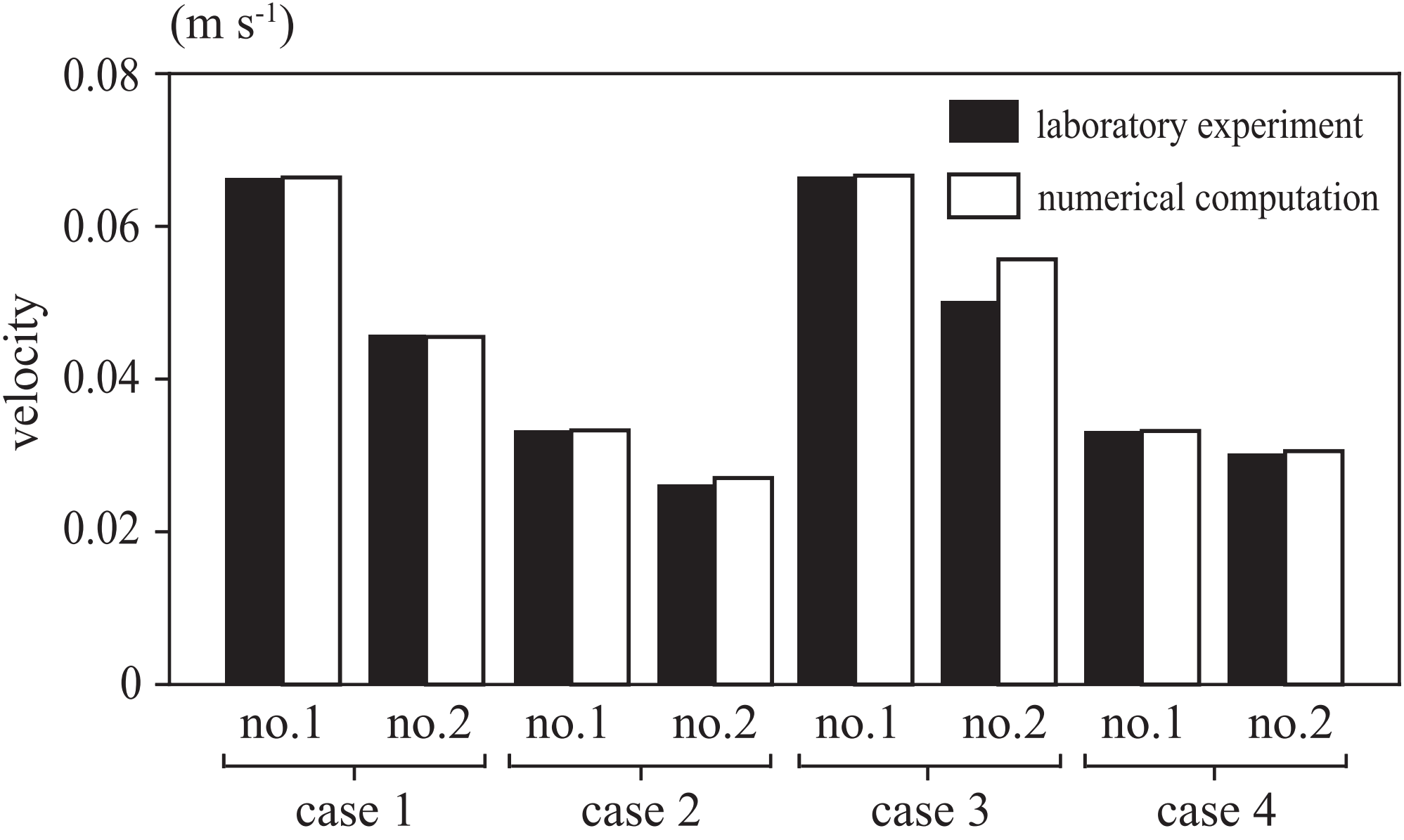
(m s-1)
0.08
0.06
0.04
0.02
0
velocity
laboratory experiment
numerical computation
no.1
no.2
no.1
no.2
no.1
no.2
no.1
no.2
case 1
case 2
case 3
case 4

Figure 6.

(a) case Lab1

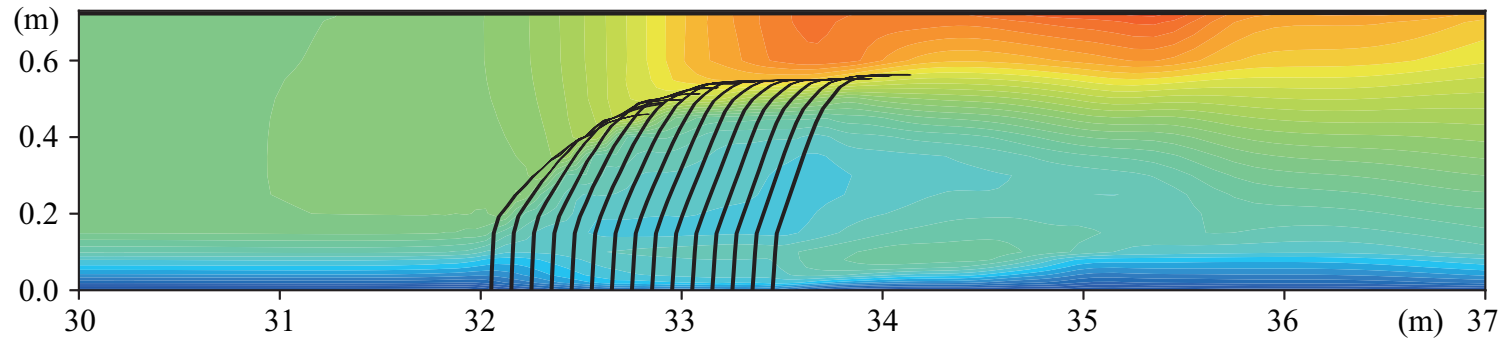

(b) case E_S

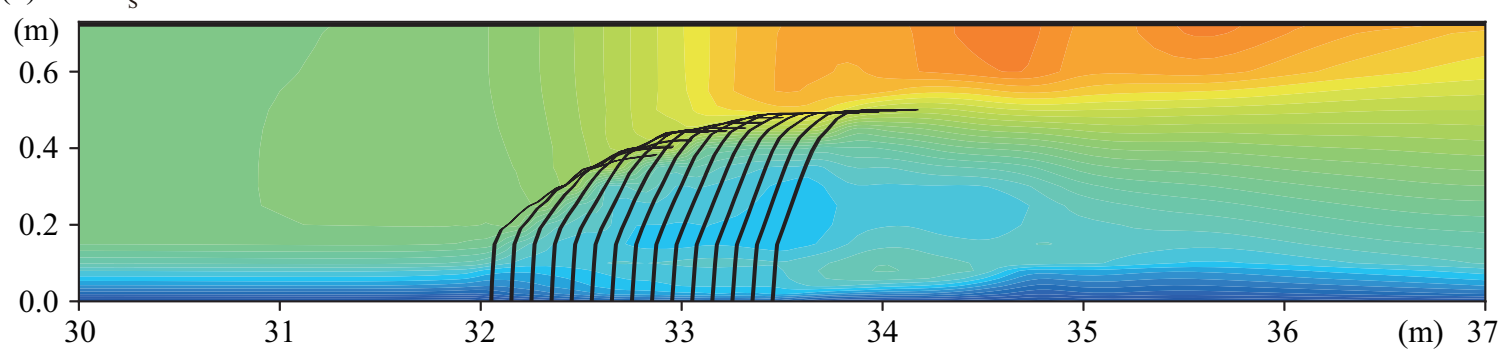

(c) case E_L

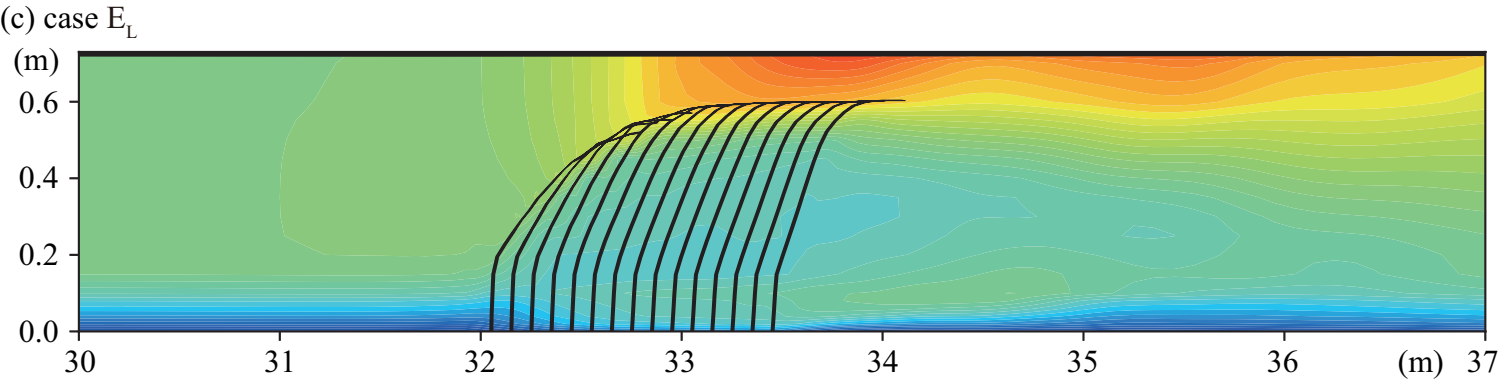

(d) case Cd_S

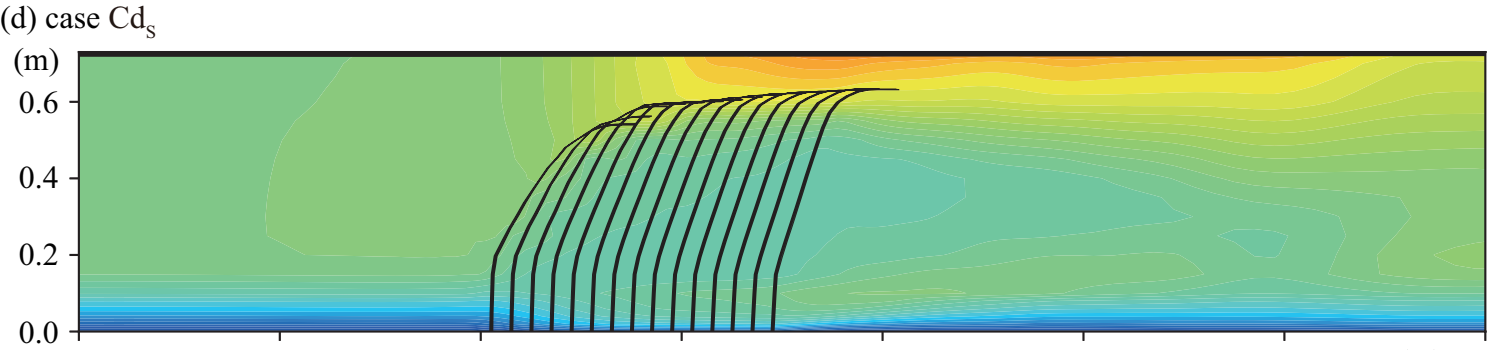

(e) case Cd_L

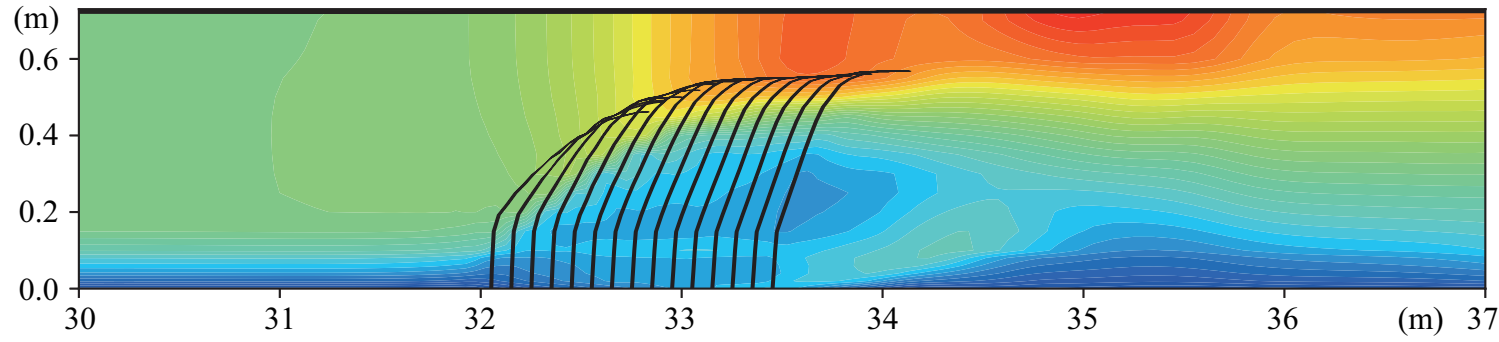

(f) case fc_S

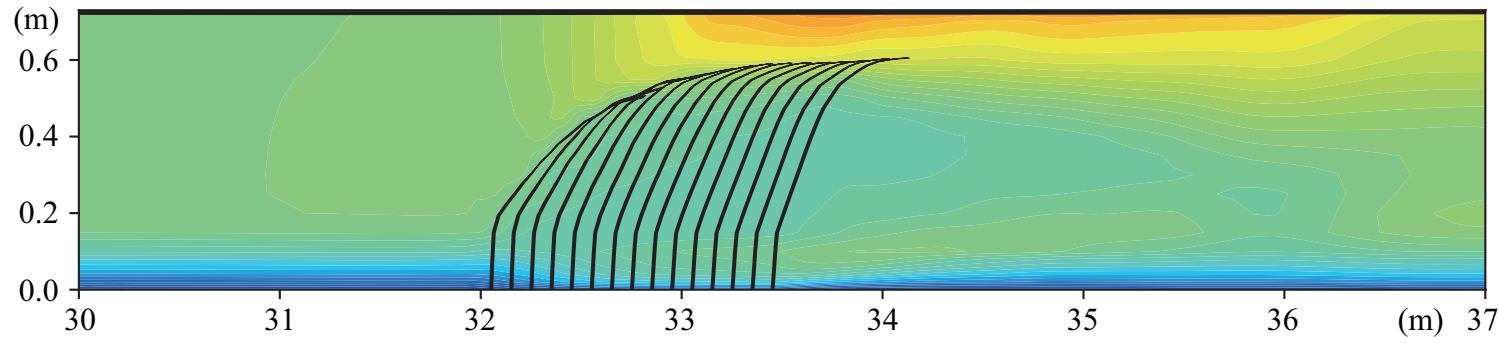

(g) case fc_L

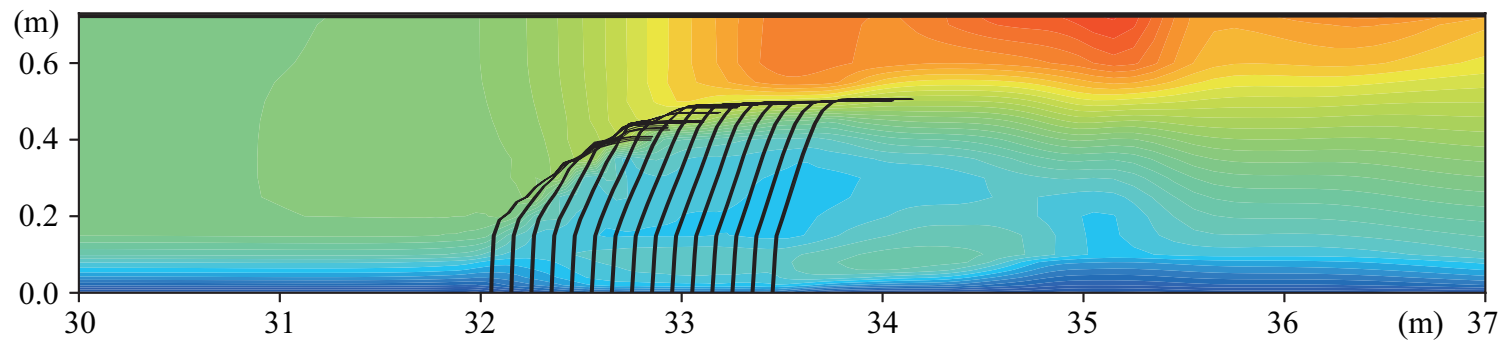

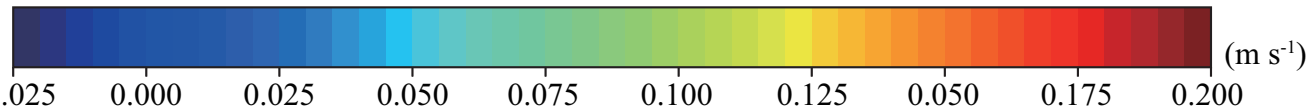

Figure 7.

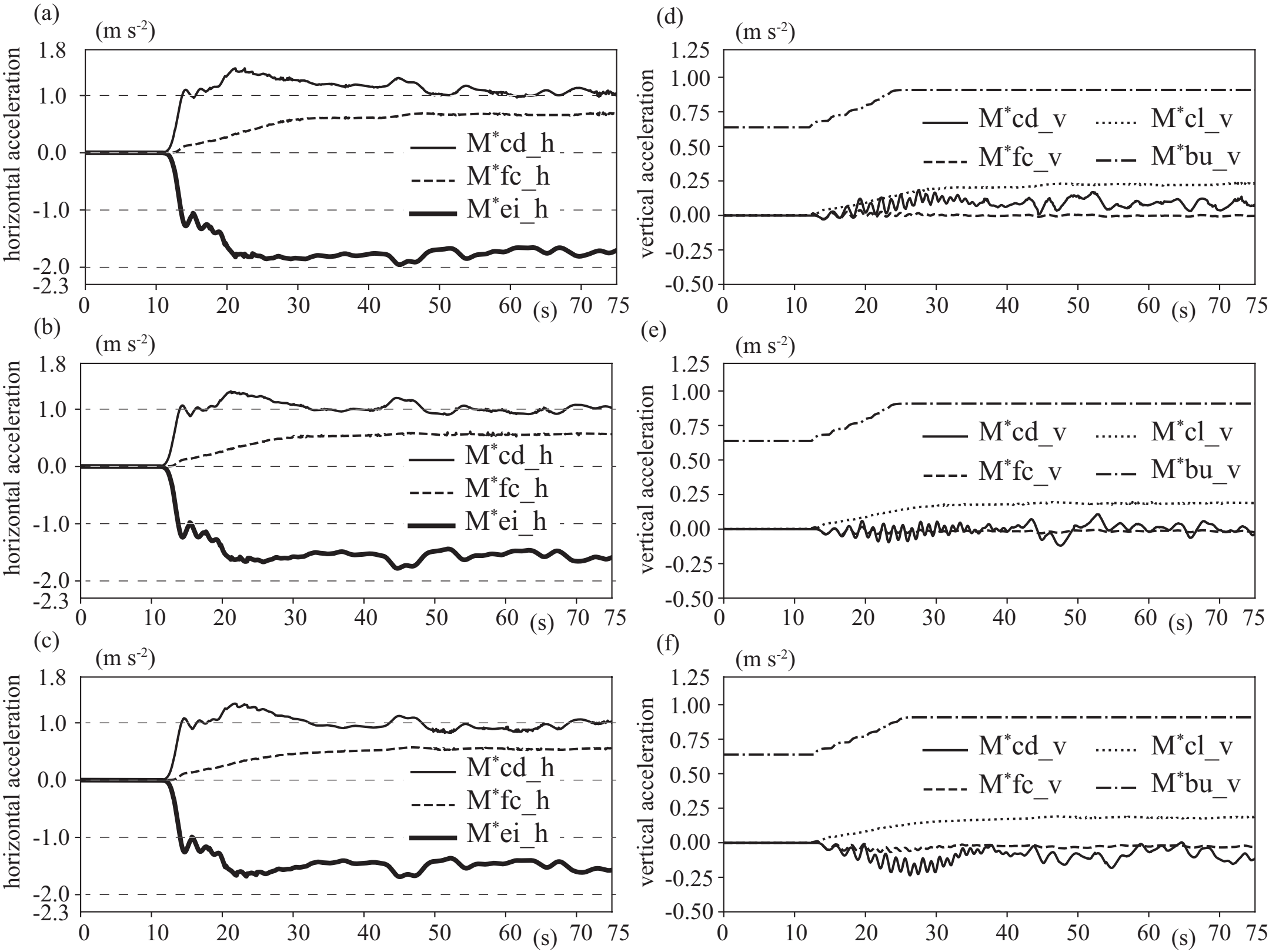
(a)
(m s-2)
horizontal acceleration
1.8
1.0
0.0
-1.0
-2.0
-2.3
M*cd_h
M*fc_h
M*ei_h
0
10
20
30
40
50
60
(s)
70
75
(b)
(m s-2)
horizontal acceleration
1.8
1.0
0.0
-1.0
-2.0
-2.3
M*cd_h
M*fc_h
M*ei_h
0
10
20
30
40
50
60
(s)
70
75
(c)
(m s-2)
horizontal acceleration
1.8
1.0
0.0
-1.0
-2.0
-2.3
M*cd_h
M*fc_h
M*ei_h
0
10
20
30
40
50
60
(s)
70
75
(d)
(m s-2)
vertical acceleration
1.25
1.00
0.75
0.50
0.25
0.00
-0.25
-0.50
M*cd_v
M*cl_v
M*fc_v
M*bu_v
0
10
20
30
40
50
60
(s)
70
75
(e)
(m s-2)
vertical acceleration
1.25
1.00
0.75
0.50
0.25
0.00
-0.25
-0.50
M*cd_v
M*cl_v
M*fc_v
M*bu_v
0
10
20
30
40
50
60
(s)
70
75
(f)
(m s-2)
vertical acceleration
1.25
1.00
0.75
0.50
0.25
0.00
-0.25
-0.50
M*cd_v
M*cl_v
M*fc_v
M*bu_v
0
10
20
30
40
50
60
(s)
70
75

Figure 8.

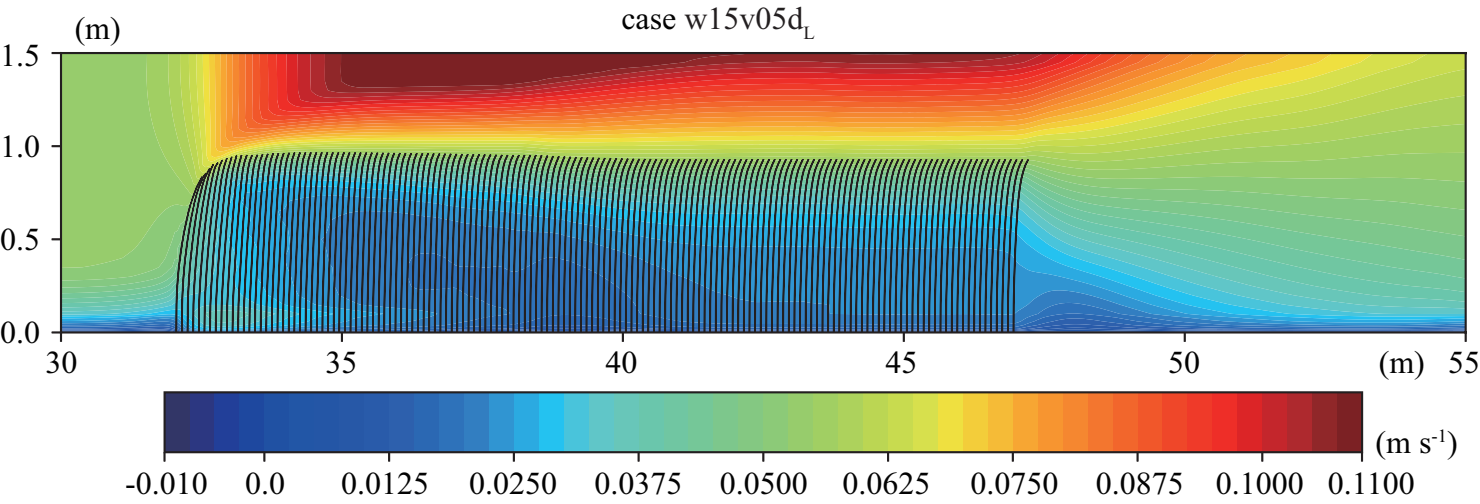
case w15v05d_L
(m)
1.5
1.0
0.5
0.0
30
35
40
45
50
(m)
55
(m s-1)
-0.010
0.0
0.0125
0.0250
0.0375
0.0500
0.0625
0.0750
0.0875
0.1000
0.1100

Figure 9.

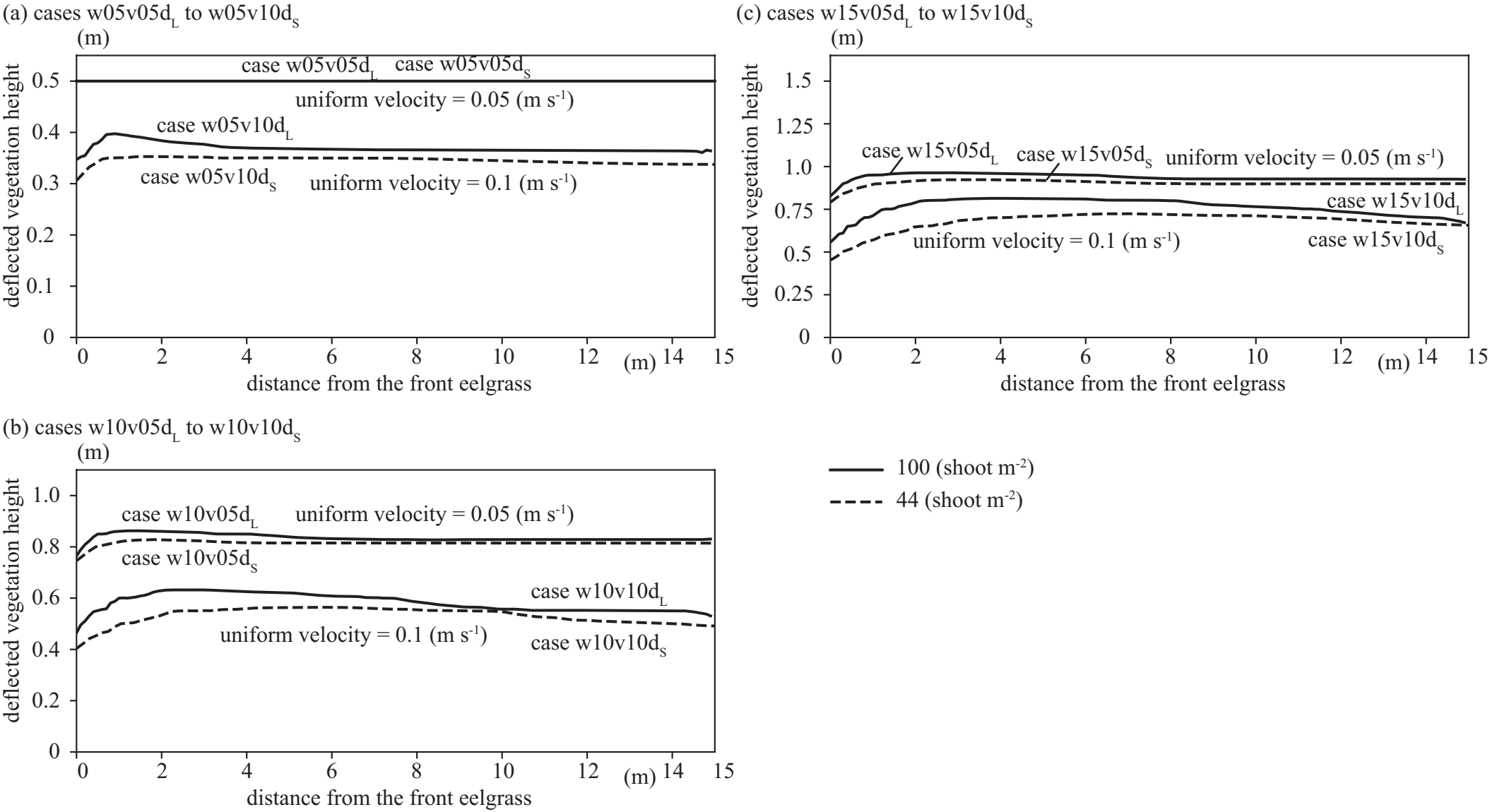
(a) cases w05v05d$_L$ to w05v10d$_S$
(m)
deflected vegetation height
case w05v05d$_L$
case w05v05d$_S$
uniform velocity = 0.05 (m s^{-1})
case w05v10d$_L$
case w05v10d$_S$
uniform velocity = 0.1 (m s^{-1})
0
0.1
0.2
0.3
0.4
0.5
0
2
4
6
8
10
12
(m)
14
15
distance from the front eelgrass
(c) cases w15v05d$_L$ to w15v10d$_S$
(m)
deflected vegetation height
case w15v05d$_L$
case w15v05d$_S$
uniform velocity = 0.05 (m s^{-1})
case w15v10d$_L$
uniform velocity = 0.1 (m s^{-1})
case w15v10d$_S$
0
0.25
0.5
0.75
1.0
1.25
1.5
0
2
4
6
8
10
12
(m)
14
15
distance from the front eelgrass
(b) cases w10v05d$_L$ to w10v10d$_S$
(m)
deflected vegetation height
case w10v05d$_L$
uniform velocity = 0.05 (m s^{-1})
case w10v05d$_S$
case w10v10d$_L$
uniform velocity = 0.1 (m s^{-1})
case w10v10d$_S$
0
0.2
0.4
0.6
0.8
1.0
0
2
4
6
8
10
12
(m)
14
15
distance from the front eelgrass
100 (shoot m^{-2})
44 (shoot m^{-2})

Figure 10.

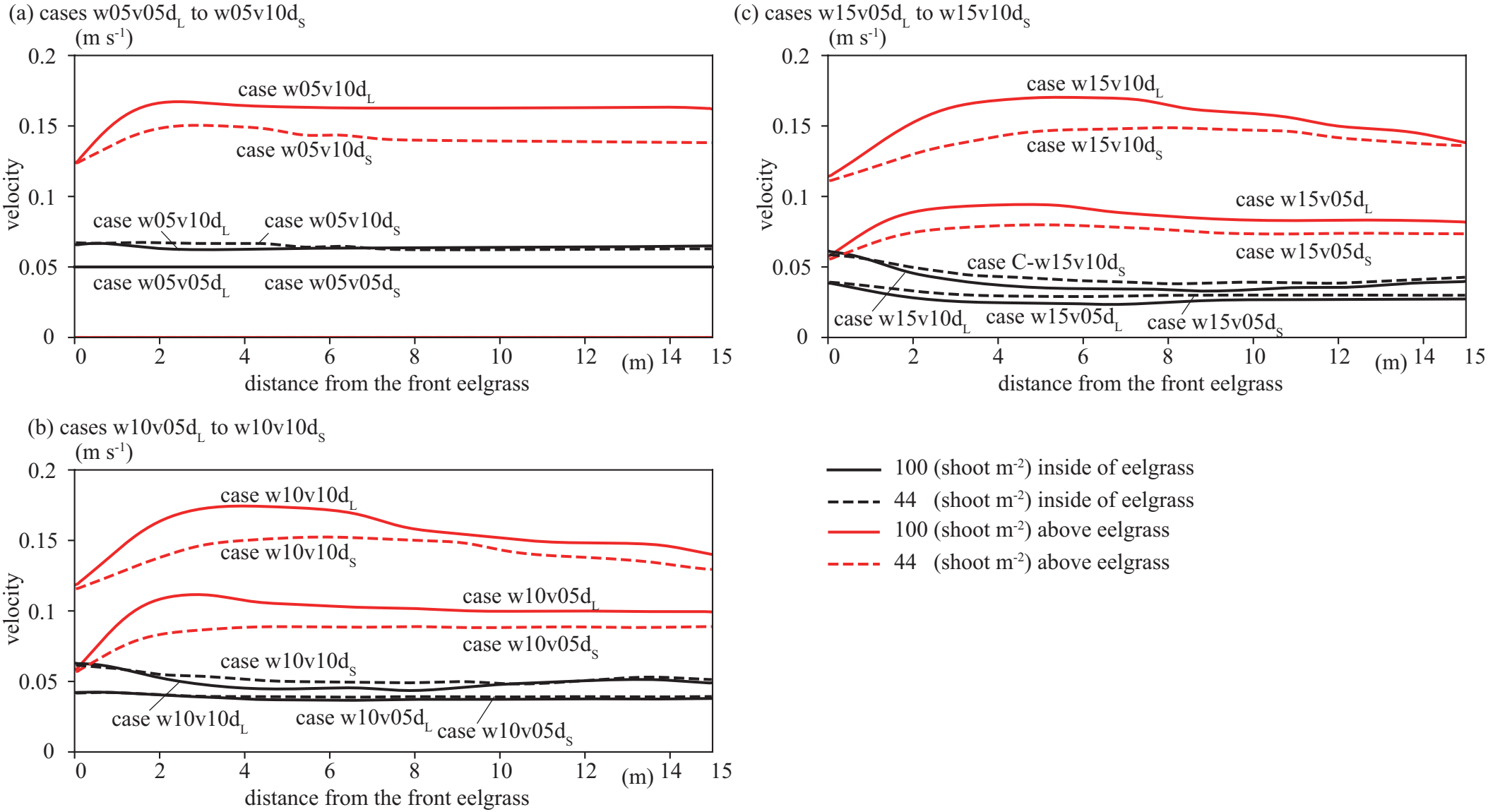
(a) cases w05v05d$_L$ to w05v10d$_S$
(m s^{-1})
velocity
distance from the front eelgrass
(m)
case w05v10d$_L$
case w05v10d$_S$
case w05v10d$_L$
case w05v10d$_S$
case w05v05d$_L$
case w05v05d$_S$
(b) cases w10v05d$_L$ to w10v10d$_S$
(m s^{-1})
velocity
distance from the front eelgrass
(m)
case w10v10d$_L$
case w10v10d$_S$
case w10v05d$_L$
case w10v05d$_S$
case w10v10d$_S$
case w10v10d$_L$
case w10v05d$_L$
case w10v05d$_S$
(c) cases w15v05d$_L$ to w15v10d$_S$
(m s^{-1})
velocity
distance from the front eelgrass
(m)
case w15v10d$_L$
case w15v10d$_S$
case w15v05d$_L$
case w15v05d$_S$
case C-w15v10d$_S$
case w15v10d$_L$
case w15v05d$_L$
case w15v05d$_S$
100 (shoot m^{-2}) inside of eelgrass
44 (shoot m^{-2}) inside of eelgrass
100 (shoot m^{-2}) above eelgrass
44 (shoot m^{-2}) above eelgrass

Figure 11.

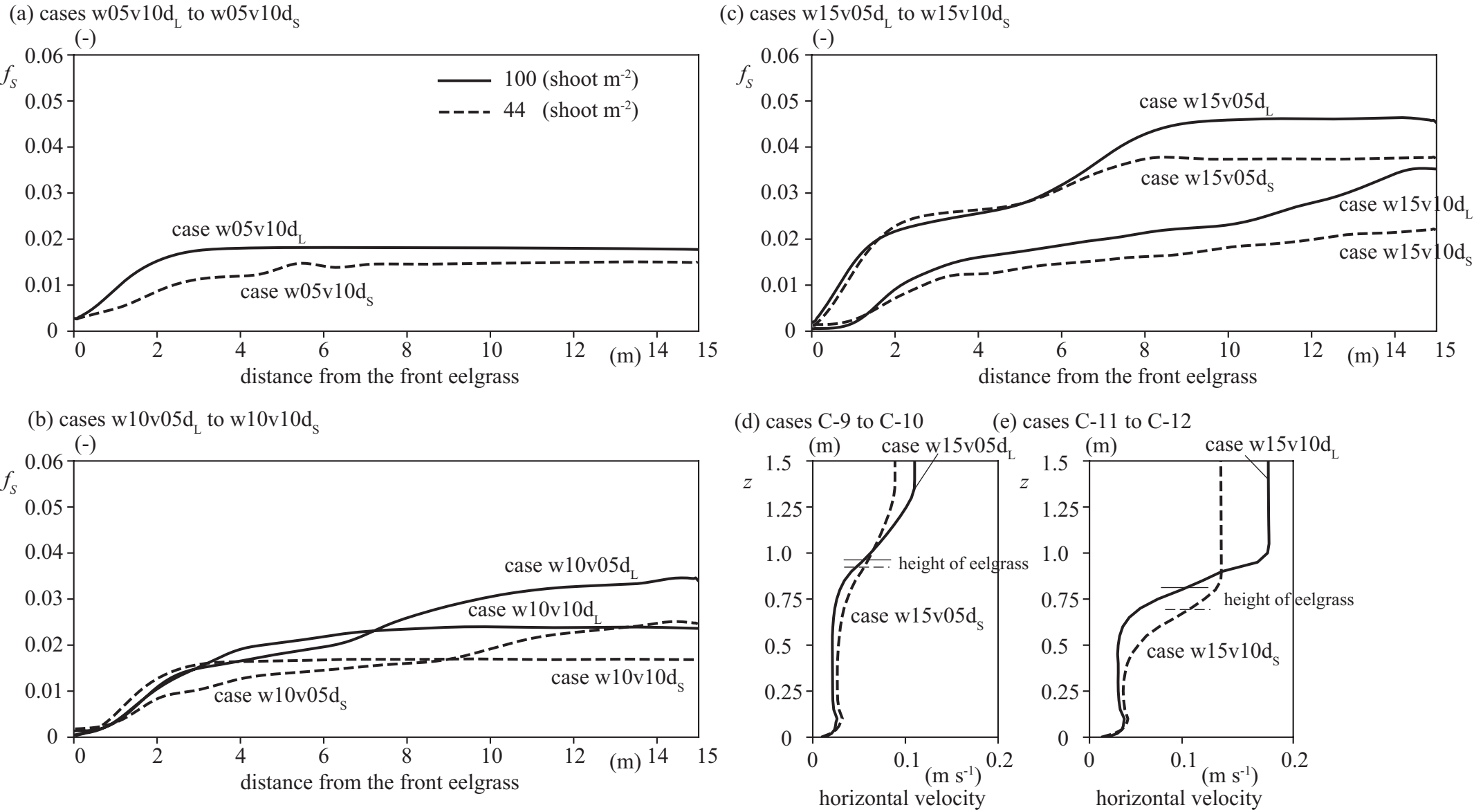
(a) cases w05v10d_L to w05v10d_S
(-)
f_S
100 (shoot m^-2)
44 (shoot m^-2)
case w05v10d_L
case w05v10d_S
(m)
distance from the front eelgrass
(c) cases w15v05d_L to w15v10d_S
case w15v05d_L
case w15v05d_S
case w15v10d_L
case w15v10d_S
(b) cases w10v05d_L to w10v10d_S
case w10v05d_L
case w10v10d_L
case w10v10d_S
case w10v05d_S
(d) cases C-9 to C-10
(e) cases C-11 to C-12
z
height of eelgrass
(m s^-1)
horizontal velocity

Figure 12.

(a) case w15v05d$_L$ without seagrass motion

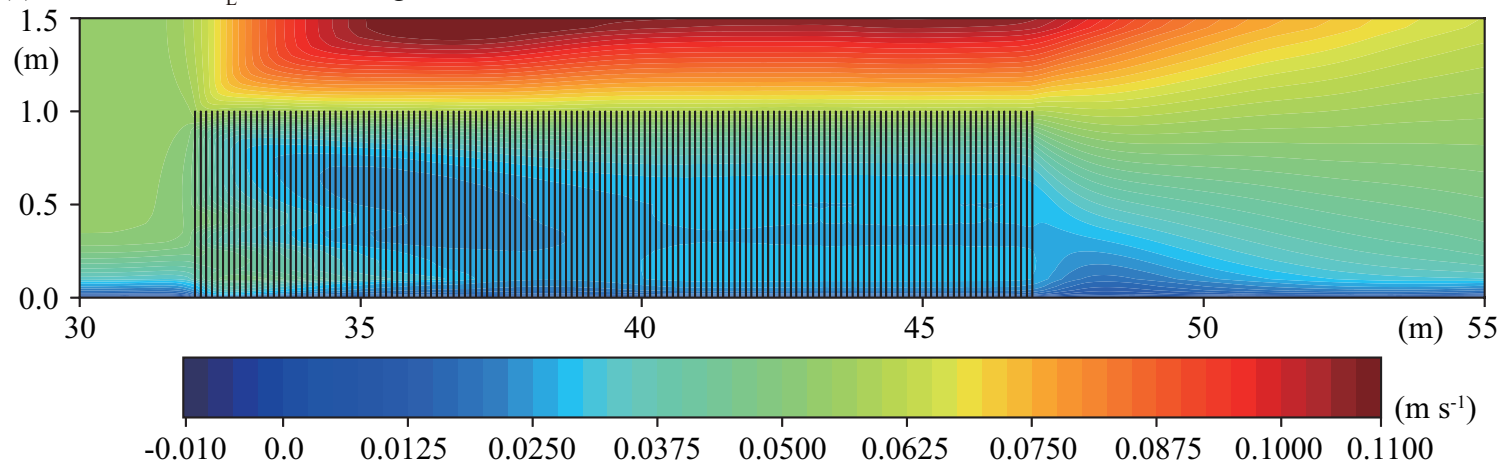

(b) difference of horizontal velocity with - without seagrass motion in case w15v05d$_L$

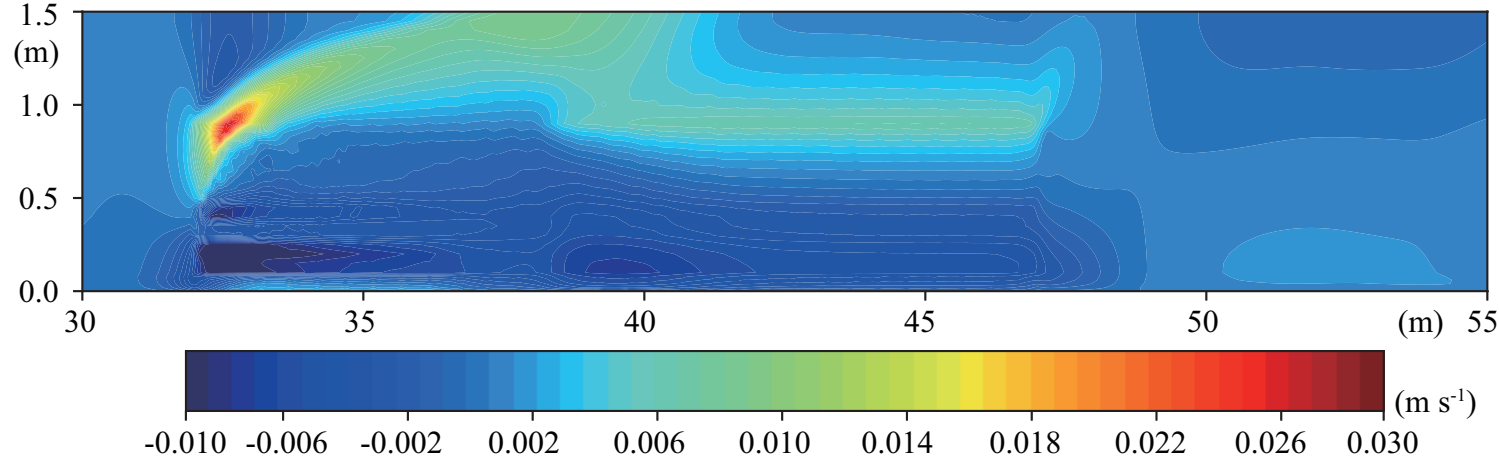

(c) friction coefficient for case w15v05d$_L$ with and without seagrass motion